VYSOKÉ UČENÍ TECHNICKÉ V BRNĚ
BRNO UNIVERSITY OF TECHNOLOGY

FAKULTA STROJNÍHO INŽENÝRSTVÍ
ÚSTAV FYZIKÁLNÍHO INŽENÝRSTVÍ

FACULTY OF MECHANICAL ENGINEERING
INSTITUTE OF PHYSICAL ENGINEERING

INFRARED MAGNETO-SPECTROSCOPY OF THE RASHBA-TYPE SEMICONDUCTORS

DIPLOMOVÁ PRÁCE
MASTER'S THESIS

AUTOR PRÁCE
AUTHOR

Bc. MAREK ŠIKULA

BRNO 2015

VYSOKÉ UČENÍ TECHNICKÉ V BRNĚ

BRNO UNIVERSITY OF TECHNOLOGY

FAKULTA STROJNÍHO INŽENÝRSTVÍ
ÚSTAV FYZIKÁLNÍHO INŽENÝRSTVÍ

FACULTY OF MECHANICAL ENGINEERING
INSTITUTE OF PHYSICAL ENGINEERING

INFRARED MAGNETO-SPECTROSCOPY OF THE RASHBA-TYPE SEMICONDUCTORS

INFRAČERVENÁ MAGNETO-SPEKTROSKOPIE POLOVODIČŮ RASHBOVA TYPU

DIPLOMOVÁ PRÁCE
MASTER'S THESIS

AUTOR PRÁCE — Bc. MAREK ŠIKULA
AUTHOR

VEDOUCÍ PRÁCE — RNDr. MILAN ORLITA, Ph.D.
SUPERVISOR

BRNO 2015

Vysoké učení technické v Brně, Fakulta strojního inženýrství

Ústav fyzikálního inženýrství
Akademický rok: 2014/2015

ZADÁNÍ DIPLOMOVÉ PRÁCE

student(ka): Bc. Marek Šikula

který/která studuje v **magisterském navazujícím studijním programu**

obor: **Fyzikální inženýrství a nanotechnologie (3901T043)**

Ředitel ústavu Vám v souladu se zákonem č.111/1998 o vysokých školách a se Studijním a zkušebním řádem VUT v Brně určuje následující téma diplomové práce:

Infračervená magneto-spektroskopie polovodičů Rashbova typu

v anglickém jazyce:

Infrared magneto-spectroscopy of the Rashba-type semiconductors

Stručná charakteristika problematiky úkolu:

Cílem diplomové práce je experimentální a teoretická studie polovodičů s obřím spinovým štěpením Rashbova typu jak valenčního, tak i vodivostního pásu. Tento typ materiálů má značný potenciál pro aplikace v elektronice a spintronice.

Cíle diplomové práce:

BiTeX materiály (X = I, Cl, Br) budou studovány ve spolupráci s Laboratoire National des Champs Magnétiques Intenses, CNRS, v Grenoblu metodou infračervené magneto-spektroskopie a dalšími doplňujícími experimentálními metodami (magneto-transportní měření, případně EPR). Tyto experimenty poskytnou detailní představu o magneto-optických vlastnostech a tudíž také o elektronové pásové struktuře těchto systémů. Experimentálně naměřená magneto-optická odezva bude srovnána s teoretickým modelem vycházejícím z jednoduchého Rashbova hamiltonianu v rámci Kubo-Greenwoodova formalismu. Tento přístup nám umožní najít limity platnosti jednoduchého Rashbova modelu, který je v současnosti nejvíce používaným k popisu BiTeX materiálů.

Seznam odborné literatury:

[1] S. Picozzi, Frontiers in Physics 2, 10 (2014).
[2] G. Landolt et al., New Journal of Physics 15, 085022 (2013).
[3] Y. L. Chen et al., Nature Physics 9, 704 (2014).
[4] H. Murakawa et al., Science 342, 1490 (2013).
[5] L. Demko et al., Physical Review Letters 109, 167401 (2012).
[6] S. Bordacs et al., Physical Review Letters 111, 166403 (2013).

Vedoucí diplomové práce: RNDr. Milan Orlita, Ph.D.

Termín odevzdání diplomové práce je stanoven časovým plánem akademického roku 2014/2015.

V Brně, dne 21.11.2014

L.S.

prof. RNDr. Tomáš Šikola, CSc. Ředitel ústavu	doc. Ing. Jaroslav Katolický, Ph.D. Děkan fakulty

ABSTRACT

Optical response of BiTeX (X = I, Cl, Br) semiconductors with a giant Rashba-type spin splitting is studied at low temperatures up to high magnetic fields applied in the Faraday configuration. Unlike the reflection configuration, the transmission configuration allows us to directly observe a set of inter-Landau level transitions in the vicinity of the crossing point of the conduction bands - Dirac point. Optical response of BiTeX compounds is compared with that expected theoretically, calculated using a simple Rashba-type Hamiltonian within Kubo-Greenwood formalism.

KEYWORDS

BiTeX compounds, giant Rashba-type spin splitting, Landau levels, infrared magneto-spectroscopy

ABSTRAKT

Optická odezva BiTeX (X = I, Cl, Br) polovodičových materiálů s obřím spinovým štěpením Rashbova typu je studována za nízkých teplot do vysokých magnetických polí, kde je směr magnetické indukce kolmý na povrch vzorku (Faradayova konfigurace). Na rozdíl od reflexního uspořádání nám transmisní uspořádání umožňuje přímé pozorování přechodů mezi Landauovými hladinami v blízkosti křižiště vodivostních pásů - Diracův bod. Optická odezva BiTeX sloučenin je srovnána s teoretickým modelem spočteným v rámci Kubo-Greenwoodova formalismu z Rashbova hamiltonianu.

KLÍČOVÁ SLOVA

BiTeX sloučeniny, obří spinové štěpení Rashbova typu, Landauovy hladiny, infračervená magneto-spektroskopie

ŠIKULA, Marek. *Infrared magneto-spectroscopy of the Rashba-type semiconductors*: master's thesis. Brno: Brno University of Technology, Faculty of Mechanical Engineering, Institute of Physical Engineering, 2015. 61 p. Supervised by RNDr. Milan Orlita, Ph.D.

DECLARATION

I declare that I have elaborated my master's thesis on the theme of "Infrared magneto-spectroscopy of the Rashba-type semiconductors" independently, under the supervision of the master's thesis supervisor and with the use of technical literature and other sources of information which are all quoted in the thesis and detailed in the list of literature at the end of the thesis.

As the author of the master's thesis I furthermore declare that, concerning the creation of this master's thesis, I have not infringed any copyright. In particular, I have not unlawfully encroached on anyone's personal copyright and I am fully aware of the consequences in the case of breaking Regulation § 11 and the following of the Copyright Act No 121/2000 Vol., including the possible consequences of criminal law resulted from Regulation § 152 of Criminal Act No 140/1961 Vol.

Brno ....

(author's signature)

Acknowledgement

I would like to thank my supervisor Milan Orlita for being patient with me, answering every single question of mine and the proof-reading. My sincere gratitude belongs also to Dr. Marek Potemski and his group who treated me as a regular member of their group in Grenoble and provided me with an experience in the field of magneto-optical spectroscopy. I also thank to many colleagues for the inspiring discussions, namely to Dr. Karol Nogajewski (Exfoliation Expert), Dr. Sándor Bordács (Hungarian Researcher and Climbing Lover) and Dr. Gérard Martinez (Emeritus Researcher and Chief Supplier of the Croissants in one person). The work would not be possible without crystals provided by Dr. Michael V. Yakushev and his kind help with experiments and data interpretation. Big thanks belong to all great people at the Institute of Physical Engineering in Brno, my wonderful classmates, Ing. Pavel Procházka, who helped me with the magneto-transport measurements, and to Doc. Radek Kalousek with Anna Russell for the text corrections. Last but not least, I would like to thank my family, who have over the years supported and guided me in my endeavors, as well as to my gorgeous girlfriend for their love.

Věnováno rodičům a Mišce. Díky za podporu.

CONTENTS

1 INTRODUCTION

The Rashba-type spin splitting (RSS) has attracted much attention in past few years. Electronic band structures showing RSS in the two dimensional electron systems (2DESs) were extensively explored with a broad variety of experiments such as *ab-initio* calculations, angle resolved photoemission spectroscopy (ARPES) [1,2], optical spectroscopy [3] and electric transport (Shubnikov-de Haas oscillations) [4,5]. Most recently, a giant RSS was discovered in BiTeX compounds (X = I, Cl, Br) [6]. Apart from their possible use in spintronic devices, BiTeX materials also show interesting properties which once again push our knowledge further. They belong to a group of 3D systems which show the giant RSS of both conduction and valence bands. This phenomenon gives rise to appearance of massless Dirac fermions and extraordinary Landau level spectrum. All the techniques listed above have been used to explore the band structure of BiTeX materials. Optical spectroscopy as a probing technique is a powerful tool for exploring bulk band structure in all its beauty and thus gives complex information about this system. So far optical magneto-spectroscopy of the BiTeX materials has been done in the reflection configuration [7] and the transmission configuration [8] which is often much easier to interpret as compared to the reflectivity data. However, the experiments in trasmission configuration were carried out at zero magnetic field, with the samples of only 10-15 μm thickness which prevent experiments in middle infrared spectral range due to non-Drude like absorption[1]. This thesis fills that gap.

The following text focuses on the theoretical and experimental study of the BiTeX materials. This thesis provides an insight into the magneto-optical properties of these materials and its structure is following: We will start with an introduction to Rashba-type systems in Chapter 2 which involves discussion of a simple Rashba model used to describe these systems. We will also explore examples of the LLs in different systems. Chapter 3 involves the history, the crystal and the band structures of the BiTeX materials. Since the preparation of specimens is a very important part of the experimental work, Chapter 4 is devoted to the description of the used techniques. Examples of the experimental data are presented in Chapter 5, followed by a qualitative interpretation of the transmission spectra in Chapter 6. Limits of the simple Rashba model are discussed in Chapter 7.

A major part of this thesis is a summary of the author's work during his Erasmus research internship at the Laboratoire National des Champs Magnétiques Intenses - LNCMI, under the auspices of CNRS Grenoble, France.

[1]Non-Drude like absorption is the absorption on free carriers in the systems defined by Rashba Hamiltonian, see Sec. 4.1.

2 SYSTEMS WITH THE RASHBA-TYPE SPIN SPLITTING

Electron paramagnetic resonance spectroscopy (EPR) was one of the first experimental methods used to probe spin splitting of the electronic states and it is dated back to 1944. The spin splitting of either bulk or surface electronic states has been studied in condensed matter physics for decades. The first mention of the zero field case dates to 1960s, when Ukrainian theoretical physicist Emmanuel I. Rashba (b.1927) contributed to semiconductor physics by the description of an interesting phenomenon, nowadays referred to as the Rashba effect in his honour [9]. The Rashba effect is a momentum-dependent spin splitting of electronic bands in condensed matter systems even at zero magnetic field. Bands with opposite spin polarization are shifted by the momentum $\vec{k}_{\mathrm{R}}$ in opposite directions. A prerequisite for the Rashba effect is the large atomic spin-orbit interaction (SOI) in a system which lacks inversion symmetry [10]. These conditions are fullfilled most typically for 2DESs. Therefore the Rashba-type spin splitting (RSS) appears in the systems, such as metal surfaces [11, 12], metallic surface alloys [2], interface of semiconductor heterostructures [13] and also the surface of topological insulators [7]. The RSS of the 2DESs promises a basis for theoretically proposed spintronic devices where the spin manipulation via an applied electric field is required; for instance, as in case of Datta-Das spin transistor [14]. Nevertheless, the size of the RSS is considered to be relatively small (at most units of meV) for most of these systems, with few exceptions, e.g., noble metal based Bi-surface alloys for which ARPES has revealed RSS of the order of 200 meV [2]. A small size of the RSS together with the need of cryogenic temperatures for device functionality and utilization of an ultrahigh purity material to avoid spin-flip scattering events [1] hinders the realization of these devices in practice [10].

The twofold spin degeneracy of electron states is a combined effect of the inversion symmetry in space and time. In other words, the time reversal symmetry leads to the restriction [15]:

$$E(\vec{k},\uparrow) = E(-\vec{k},\downarrow), \tag{2.1}$$

where the energy of a spin-up electron with momentum $\vec{k}$ equals that of the spin-down electron with momentum $-\vec{k}$. In quantum mechanics, the systems with the time reversal symmetry and half-integer total spin have often doubly degenerated energy levels which is also known as Kramer's degeneracy. This appears when the lattice also has inversion symmetry (translational operation $\vec{r} \to -\vec{r}$ does not change the crystal lattice), one obtains second condition:

$$E(\vec{k},\uparrow) = E(-\vec{k},\uparrow). \tag{2.2}$$

By the combination of Eq. (2.1) and Eq. (2.2), one can clearly see that band structure must fullfill:

$$E(\vec{k},\uparrow) = E(\vec{k},\downarrow), \tag{2.3}$$

thus the energy does not depend on the electron spin orientation. Nevertheless, if the crystal lattice lacks the inversion symmetry, we have to assume the possibility that:

$$E(\vec{k},\uparrow) \neq E(\vec{k},\downarrow), \tag{2.4}$$

i.e., spin degeneracy is lifted. At zero magnetic field, the SOI is one of the candidates to lift the spin degeneracy. In order to fully understand origin of the RSS, a simple free electron model, which describes 2DESs with SOI, is employed.

2.1 Simple Rashba model at zero field

The very simple example of the SOI is a 2D system with the Hamiltonian containing perturbation [16]:

$$H = \frac{p^2}{2m} + H_{\mathrm{R}}, \tag{2.5}$$

where H_{R} is the Rashba Hamiltonian[1]

$$H_{\mathrm{R}} = \alpha_{\mathrm{R}}(\vec{e}_z \times \vec{k}) \cdot \vec{\sigma}, \tag{2.6}$$

where α_{R} denotes Rashba coupling parameter, m is taken to be the effective mass, $\vec{e}_z$ is the unit vector in the z-direction, $\vec{k} = (k_x, k_y, 0)$ is the wavevector, $\vec{p} = (p_x, p_y, 0)$ and $\vec{\sigma}$ are the momentum and spin vectors, respectively.

A solution to Schrödinger's equation with the Hamiltonian Eq. (2.5) can be found through further analysis. It was shown, see e.g., [16], that the parabolic dispersion will be split in two parabolas, shifted in xy plane by energy of $\alpha_{\mathrm{R}}k$ and having energies:

$$E_{1,2} = \frac{\hbar^2 k^2}{2m} \pm \alpha_{\mathrm{R}} k, \tag{2.7}$$

[1]Which is nothing but a two-dimensional version of the Dirac Hamiltonian (with a 90 degrees rotation of the spins).

where $\hbar$ is the reduced Planck constant. The calculated wave functions have the following form [16]:

$$\psi_1(\vec{r}) = \exp(i\vec{k}\cdot\vec{r})(|\uparrow\rangle + i\exp(i\theta_k)\,|\downarrow\rangle) \qquad \text{for} \qquad E_1 = \frac{\hbar^2 k^2}{2m} + \alpha_{\mathrm{R}} k, \tag{2.8}$$

$$\psi_2(\vec{r}) = \exp(i\vec{k}\cdot\vec{r})(i\exp(i\theta_k)\,|\uparrow\rangle + |\downarrow\rangle) \qquad \text{for} \qquad E_2 = \frac{\hbar^2 k^2}{2m} - \alpha_{\mathrm{R}} k, \tag{2.9}$$

where θ_k is an angle between $\vec{k}$ and x-axis. For $k \approx 0$ we obtain energy linearly dependent on k, thus resembling a massless nature of particles; therefore, we may define Fermi velocity as $v_{\mathrm{F}} = \alpha_{\mathrm{R}}/\hbar$.

Equations (2.8) and (2.9) imply that the electrons with the same $\vec{k}$ vector and opposite spins will have different energies. Our approach using the free-electron model gives us two direct results. It correctly describes the origin of the splitting and shows that Rashba-type SOI orients the spins of propagating electrons with a certain $\vec{k}$. The results obtained using free-electron model are illustrated in Fig. 2.1. The spin orientation is always perpendicular (in-plane) to the electron momentum. The two concentric circles indicate the corresponding Fermi surfaces.

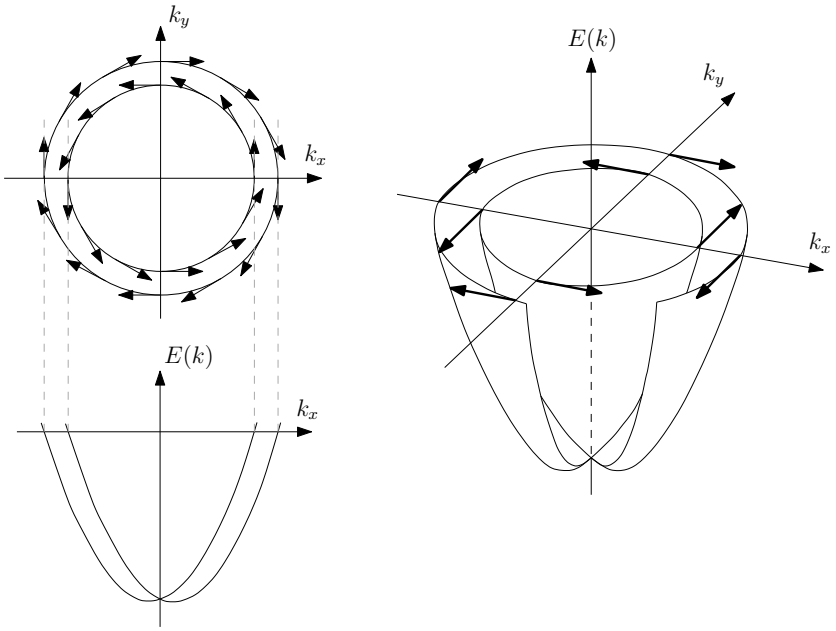

Fig. 2.1: The qualitative sketch of the energy dispersion of the free-electron state with RSS and Fermi surfaces in the upper part of the left figure. The arrows indicate the spin orientation for a given momentum $\vec{k}$. [16, 17].

Not only RSS of the surface states is object of the interest, e.g., three-dimensional (bulk) systems has been explored from the point of view of the RSS [6, 18]. These

systems show RSS with typical energies of 0.1 - 0.2 eV and can be described by the modified Hamiltonian (2.5). This Hamiltonian is extended to the third dimension by adding the term $\hbar^2 k_z^2/(2m)$. Furthermore, the possibility of controlling the carrier density by doping these systems will bring series of Rashba-split insulator, p and n-type semiconductors, and metal samples, which might also lead to the development of novel superconductors [6]. Equally promising is the perspective for the technological development and miniaturization of spintronic devices due to their higher size of the RSS, so-called giant RSS. Generally, the size of the RSS is characterized by the Rashba coupling parameter α_{R} which indicates the strength of the SOI. As was shown in a number of works, see e.g., [18], the Rashba model can be derived in the framework of the $\vec{k} \cdot \vec{p}$ theory or from the point of view of a tight binding approximation [15,16]. However, those approaches are tediously extensive, therefore we will introduce the intuitive model, which provides an insight into a theoretical background of the problem, so-called simple Rashba model. For the rigorous and thorough derivation of the Rashba model, see e.g., [17] (Sec. 6.3). The simple Rashba model underlies our experimental work and facilitates interpretation of the experimental data. Details of the calculation are left for the Appendix A. As a result of the simple mathematical treatment, we will obtain Hamiltonian in the 2×2 matrix form:

$$H = \begin{pmatrix} p^2/(2m^*) & -\mathrm{i}p^- \alpha_{\mathrm{R}}/\hbar \\ \mathrm{i}p^+ \alpha_{\mathrm{R}}/\hbar & p^2/(2m^*) \end{pmatrix}, \tag{2.10}$$

where m^* is the effective mass in units of the free electron mass, $p^+ = p_x + \mathrm{i}p_y$ and $p^- = p_x - \mathrm{i}p_y$, respectively.

2.2 Simple Rashba model in a magnetic field

By applying the Peierls substitution, one can conveniently introduce the magnetic field into the zero field Hamiltonian, Eq. (2.10) [19]. On the basis of our experimental configuration[2], the magnetic field $\vec{B} = (0, 0, B_z)$ perpendicular to the sample surface is introduced. The z-axis is later on identified as with the c-axis of BiTeX material in which the RSS appears only in the xy plane as described by Hamiltonian (2.5). In the quantum-mechanics notation, our system is equivalent to a harmonic oscillator, so let us introduce the standard creation and annihilation operators:

$$a = \sqrt{\frac{1}{2e\hbar B}}(p_x + \mathrm{i}p_x) = \sqrt{\frac{1}{2e\hbar B}}p^+, \tag{2.11}$$

[2]Our experimental work is carried out in the Faraday configuration - incident radiation propagates parallel to an externally applied magnetic field (along the c axis of the sample).

$$a^\dagger = \sqrt{\frac{1}{2e\hbar B}}(p_x - \mathrm{i}p_x) = \sqrt{\frac{1}{2e\hbar B}}p^-. \tag{2.12}$$

By applying the creation and annihilation operators on the N-th $|N\rangle$ and $(N-1)$-th $|N-1\rangle$ quantum states, we will obtain an equation in Schrödinger's form $H|\varphi\rangle = E_N|\varphi\rangle$, searching for the solution in a form of basis $\begin{pmatrix} \alpha|N\rangle \\ \beta|N-1\rangle \end{pmatrix}$:

$$\begin{pmatrix} \frac{\hbar^2 k_z^2}{2m^*} + \frac{e\hbar B}{m^*}(N+\frac{1}{2}) & -\mathrm{i}\frac{\alpha_\mathrm{R}}{\hbar}\sqrt{2e\hbar B}\sqrt{N} \\ \mathrm{i}\frac{\alpha_\mathrm{R}}{\hbar}\sqrt{2e\hbar B}\sqrt{N} & \frac{\hbar^2 k_z^2}{2m^*} + \frac{e\hbar B}{m^*}(N-\frac{1}{2}) \end{pmatrix} \begin{pmatrix} \alpha \\ \beta \end{pmatrix} = E_N \begin{pmatrix} \alpha \\ \beta \end{pmatrix}, \tag{2.13}$$

where α and β are the complex coefficients.

2.3 Landau levels

The solution of the Eq. (2.13) gives us eigenvalues:

$$E_{\pm N} = \hbar\omega_c N \pm \sqrt{\left(\frac{\hbar\omega_c}{2}\right)^2 + 2v_\mathrm{F}^2 e\hbar B N} + \frac{\hbar^2 k_z^2}{2m^*}, \tag{2.14}$$

where $\omega_c = eB/m^*$ is the cyclotron frequency and N is the positive integer. For $N = 0$, the energy is given as $E_0 = \hbar\omega_c/2$. This set of eigenvalues of the Hamiltonian H is also known as the Landau level spectrum. The Landau levels (LLs) are energy levels which reflect the quantization of the cyclotron motion of electrons subjected to a magnetic field. The effect of the quantization into the LLs might be observed when the thermal energy is smaller than the energy level separation, $kT \ll \hbar\omega_c$. However, this is not always true as seen, e.g., in [20]. From the point of view of the classical mechanics, we consider a moving electron confined to the xy plane under the uniform magnetic field pointing in z direction, Fig. 2.2.

In order to maintain the electron in the cyclotron motion, the Lorentz and the centrifugal forces have to be balanced:

$$m\frac{v^2}{r} = evB, \tag{2.15}$$

$$\omega_c = \frac{eB}{m}, \tag{2.16}$$

where v is the non-relativistic speed of the electron. Cyclotron frequency does not depend on the radius, therefore it gives us a qualitative time-scale of the problem [21].

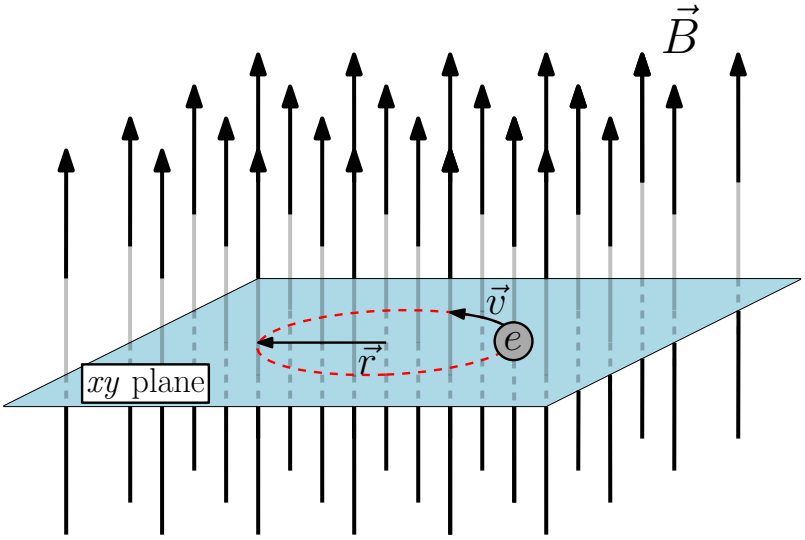

Fig. 2.2: The classical cyclotron motion of an electrically charged particle in a uniform magnetic field.

2.4 Examples of the Landau levels in other systems

2.4.1 Conventional 2D semiconductors

More simple description of the dynamics of electrons inside a material is provided within the framework of the non-relativistic quantum mechanics. 2DESs with the typical band structure consisting of a parabolic conduction band and an upside-down parabolic valence band, see Fig. 2.3: a), have in the presence of a magnetic field equally spaced LLs [22]:

$$E_N = E_\pm \pm \hbar\omega_c \left(N + \frac{1}{2}\right), \qquad N = 0, 1, 2, ... \tag{2.17}$$

where E_+ means the bottom of the conduction band E_C and E_- the top of the valence band E_V. This model is no longer valid when applied to systems with non-parabolic bands such as graphene.

2.4.2 Graphene

Graphene is a 2D monolayer of carbon atoms which are arranged into a honeycomb lattice [23]. The band structure is significantly different from conventional 2DESs with parabolic bands which has an important impact, e.g., on the LL spectrum. At two nonequivalent Brillouin zone corners (**K** and **K′**) the conduction band and the

valence band merge into so-called Dirac cone [24]. In the vicinity of the crossing point of the bands (Dirac point), see Fig. 2.3: b), energy of the electron depends linearly on its momentum:

$$E(k) = \pm v_{\mathrm{F}} \hbar k. \tag{2.18}$$

This specific band structure gives rise to massless Dirac fermions in the vicinity of the Dirac point [25]. The relativistic-like nature of the massless Dirac fermions implies for 2DESs unusual LLs. LLs follow a $\sqrt{B}$- and $\sqrt{N}$-dependence which is in a sharp contrast to the equally spaced LLs in 2DESs with parabolic bands. Moreover the $N = 0$ LL is field independent. Energy of the LLs is given as:

$$E_N = \mathrm{sgn}(N)\sqrt{2ev_{\mathrm{F}}^2|N|B}. \qquad N = ..., -2, -1, 0, 1, 2, ... \tag{2.19}$$

Generally speaking, systems with the RSS may have LLs following Eq. (2.17) for a relatively small α_{R} and a high magnetic field. Whereas for a low magnetic field and a small N LLs follow rather Eq. (2.19).

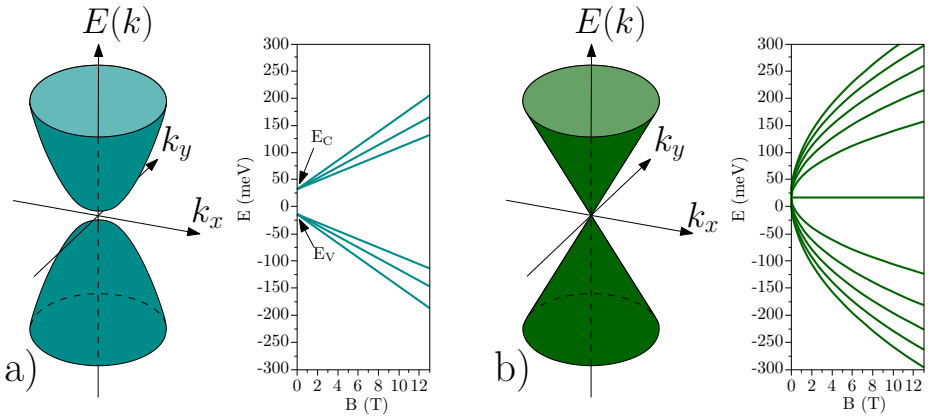

Fig. 2.3: a) The sketch of the parabolic band structure of an ordinary semiconductor and its LLs' dependence on the magnetic field. b) The sketch of the band structure of the graphene in the vicinity of the Dirac point and its LLs' dependence on the magnetic field. Partially adapted from [22].

3 BiTeX MATERIALS (X = I, Cl, Br)

BiTeX materials belong to a family of non-centrosymmetric layered 3D (bulk) semiconductors, so-called *bismuth-tellurohalides* [26]. X stands for the three elements from a group of halides, i.e., iodine (I), chlorine (Cl) and bromine (Br). Heavy constituent atoms (especially bismuth) next to the light atoms providing strong SOI are together with the inversion asymmetry of the crystal lattice at the origin of giant RSS of both conduction and valence bands. The giant RSS gives rise to appearance of the massless Dirac fermions around the **A** point of the Brillouin zone, Fig. 3.1: a). Interesting properties due to the giant RSS in these materials were discovered only recently [6], but BiTeX materials themselves are not new in condensed matter physics; in fact, they have been known for a long time.

3.1 History

To the best of our knowledge, the first mention of BiTeX materials dates back to 1951 when Dönges reported on the crystallographic studies for BiTeI derived from the parent compounds Bi_2Te_3 and BiI_3 [27]. Tomokiyo later showed the phase diagram and crystal structure of BiTeI using X-ray diffraction on a single crystal and its semi-metallic nature supported by electrical resistivity and the Hall coefficient [28]. The two remaining members of the BiTeX family were also crystallographically studied for a long period of time. Adverb "long" has its meaning, because BiTeCl was prepared for the first time in 1994, after more than 40 years since the first studies of parent material [29]. All efforts to obtain a suitable single crystal of bismuth tellurohalides were met by some serious difficulties. That is also the reason why the X-ray powder diffraction technique was used for the crystal structure determination. For direct observation of the RSS is crucial to have a single crystal. On the other hand, the single crystal of BiTeI was already prepared in 1976 [28] which is another reason why BiTeI has been considered to be a well-studied material. One would say that after 60 years of knowing and studying bismuth-tellurohalides the scientific world should know every single detail about these materials. This is not true; however, a new breakthrough soon came. A boom in search of the RSS in the BiTeX materials started in 2011 when Ishizaka and her co-workers reported on the RSS of the bulk bands of BiTeI [6]. This paper was soon followed by a report on the RSS in BiTeCl published in 2012 [10]. Furthermore, two years later, Chen and his co-workers discovered that BiTeCl displays specific surface states which are sensitive to the crystal termination. This discovery suggested the possibility that BiTeCl behaves

as a topological insulator[1] [30]. Nevertheless, nobody have found any evidence of topologically nontrivial states ever after [26, 31]. In addition to the RSS of BiTeI and BiTeCl, BiTeBr has also been studied from the same point of view. In 2012 and in great detail in 2013, Eremeev and his group have carried out calculations of the band structure of BiTeBr which has showed RSS [10,32]. The following Sections 3.2 and 3.3 summarize our current knowledge and the basic properties of the crystal and band structures of the BiTeX materials gained during past six decades.

3.2 Crystal structure

The crystal structure of the BiTeX materials has been known for a long time as was mentioned in a previous section. All three materials crystallize in a hexagonal system, but different space groups, see Tab. 3.1. The BiTeX materials are layered materials. The crystals have no inversion symmetry due to continuous stacking of the three atomic layers along the c axis and in the case of BiTeCl, four layers stacking [29].

Tab. 3.1: Clasification of the space groups and the unit cell parameters of the BiTeX materials. Cited from [29].

Material	Space group	a (Å)	c (Å)
BiTeI	$P3m1$	4.3392	6.854
BiTeBr	$P3m1$	4.2662	6.487
BiTeCl	$P6_3mc$	4.2426	12.397

All these polar compounds are characterized by the semi-ionic bonding within the layers, which are separated by a Van der Waals gap, giving rise to a quasi-2D nature [33]. As shown in Fig. 3.1: b), BiTeI is composed as a sequence of Bi, Te and I layers. This three-layer crystal has the trigonal space group of $P3m1$ for which the lack of I-symmetry is characteristic [18]. It was previously reported that the structure of BiTeBr should differ from that of BiTeI by tellurium and bromine atoms randomly distributed within the Te and Br atomic layers [10]. As a consequence, the band structure of this material was never addressed before, while the RSS was predicted only in the ordered phase of BiTeBr. Nevertheless, it was subsequently reported that a single crystal of BiTeBr grown by the chemical vapor transport

[1]Topological insulator is a material with time reversal symmetry which behaves as an insulator in its bulk. However, it also exhibits specific surface states which are conductive, thus allowing movement of the electrons along the surface.

method possessed the well-defined stacking of Te and Br triangular lattices [34], see the crystal structure in Fig. 3.1: c). In contrast to BiTeI and BiTeBr, the unit cell of BiTeCl is doubled in the c-direction, as shown in Fig. 3.1: d). Crystal is symmetric under the screw operation consisting of a non-primitive translation by $c/2$ along the c axis and a rotation of $\pi/3$ around the same axis [26].

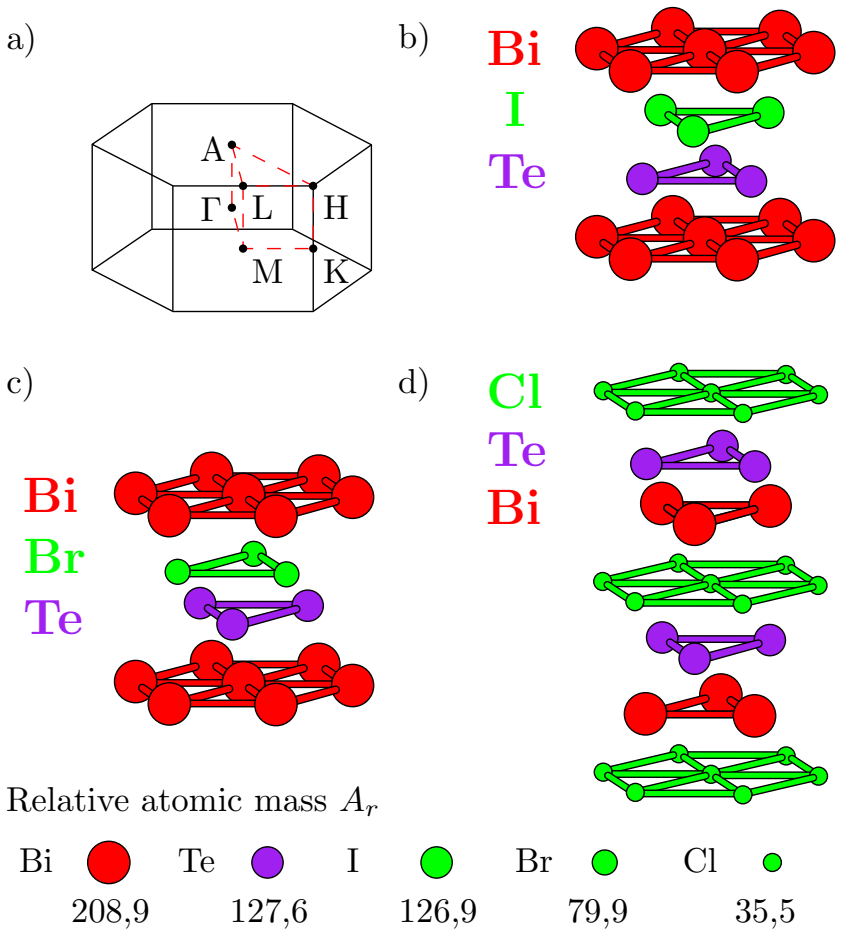

Fig. 3.1: a) Brillouin zone of the hexagonal cell. Adapted from [10]. Atomic crystal structure of b) BiTeI, c) BiTeBr, d) BiTeCl.

3.3 Electronic band structure

Initially, the band structure of BiTeX materials was calculated within the density functional theory formalism which is very often implemented in the Vienna *ab-initio* (first principle) simulation package (VASP) [10,26,32]. These calculations were subsequently followed by a wide variety of experiments, e.g., ARPES [6,34], optical spectroscopy [35, 36] and electric transport (Shubnikov-de Haas oscillations) [37].

These measurements are consistent with theoretical calculations. Calculated band structures without SOI resemble a conventional semiconductor, however taking SOI

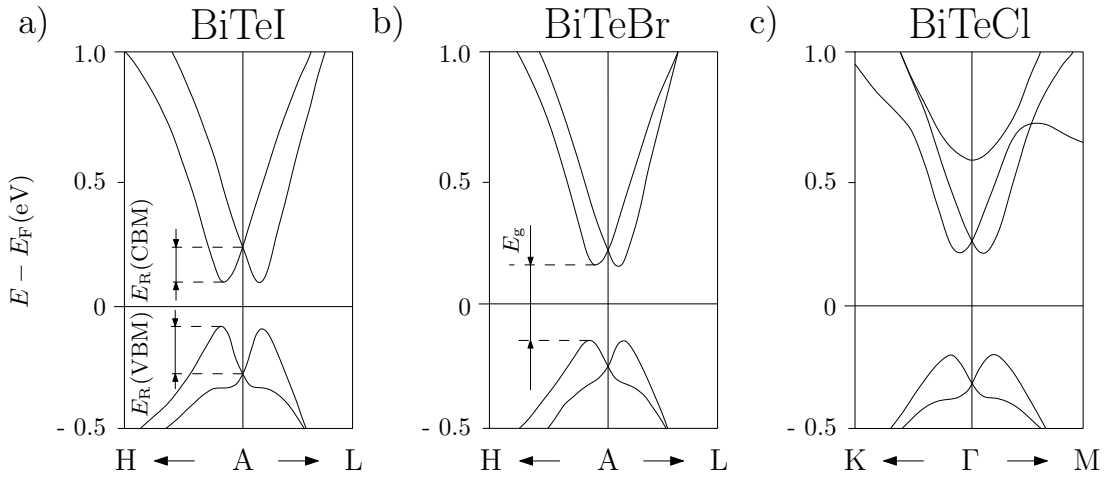

Fig. 3.2: Theoretically calculated electronic band structures of a) BiTeI, b) BiTeBr, c) BiTeCl. Adapted from [10].

into account, the RSS appears. Figure 3.2 outlines the appearance of the BiTeX band structures. Calculated electronic band structures can be found in a number of theoretical works, e.g., [6, 18, 32].

Figure 3.2: a) clearly shows that RSS of BiTeI is the largest among BiTeX materials. Actually, the size of the splitting is one of the largest ever seen in this system. One possible explanation could be the fact that iodine is the heaviest element out of three halides thus meaning bigger SOI as compared to the others. The band structure of BiTeBr, see Fig. 3.2: b), is very similar to the band structure of BiTeI. However, it has an advantage over BiTeI since its surface state is larger split off from the bulk conduction band and more isotropic [32]. The RSS of the bulk conduction band minimum (CBM) and the valence band maximum (VBM) decreases along with the increase of the band gap. BiTeBr also has a small advantage over BiTeCl with its larger RSS. In BiTeCl, see Fig. 3.2: c), the folding of the Brillouin zone along the k_z direction leads to the transfer of the band gap to the $\mathbf{\Gamma}$ point [10]. The Cl^- ion is more electronegative than Br^- or I^-, so that the states below the gap in BiTeCl are pulled lower in energy [8]. As can also be seen from Tab. 3.2, the lighter the halide atom, the wider the band gap and smaller the RSS, which is given by the Rashba energy E_R. BiTeCl has a non-trivial surface states structure which varies according to the surface termination. This is a consequence of the strong inversion asymmetry. The charge carriers on the two differently terminated surfaces become opposite types, leading to a strong bulk charge polarization. Moreover, a single Di-

rac cone was observed inside the bulk energy gap in BiTeCl, so-called in-gap surface topological state [30]. This fact could mean that BiTeCl is the first candidate for the strong polar topological insulator. The summary of the E_g and E_R values for all three materials is listed in a Tab. 3.2.

Tab. 3.2: Energy gap E_g, relative atomic mass A_r of the halides and Rashba energy E_R for the conduction band minimum (CBM) and the valence band maximum (VBM). Cited from [18, 32, 33, 38].

Material	Rel. atomic mass	E_g(meV)	E_R(CBM) (meV)	E_R(VBM) (meV)
BiTeI	A_r(I)=126,9	242	113	113
BiTeBr	A_r(Br)=79,9	310	66	111
BiTeCl	A_r(Cl)=35,5	441	30	106

3.4 Landau levels in BiTeX rising from the RSS

LLs in BiTeX compounds may be approximately described using Eq. (2.14), see Sec. 2.3. Due to the unique appearance of the band structure, which forms a single Dirac cone in the vicinity of the crossing point of the conduction bands, LL spectrum has

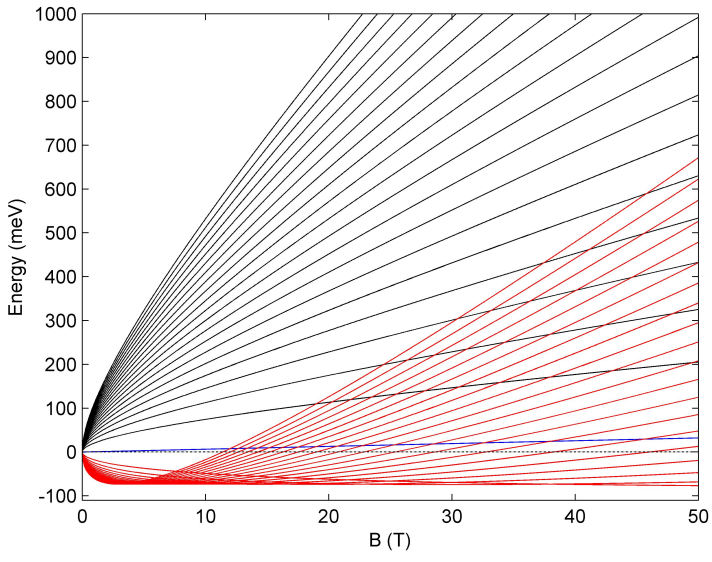

Fig. 3.3: Dispersion of the LLs in the vicinity of the crossing point (Dirac point) of the conduction bands in the BiTeX materials. The black lines denote LLs above the crossing point, the red ones below the crossing point and the blue line is $N = 0$ LL.

a specific form as compared to the LLs of conventional 2DEGs or graphene, see Fig. 2.3. The following figure is a direct representation of the Eq. (2.14). The LL spectrum has been plotted in the Fig. 3.3 for indices $N = 0, ..., 20$. The black lines denote LLs above the crossing point and are described by the Eq. (2.14) with plus sign, whereas red lines denote LLs below the crossing point and are described by the Eq. (2.14) with minus sign. The blue line is used for $N = 0$ LL. For small N and small magnetic fields, LLs are roughly proportional to $\sqrt{B}$ and become linear as N and the magnetic field increase.

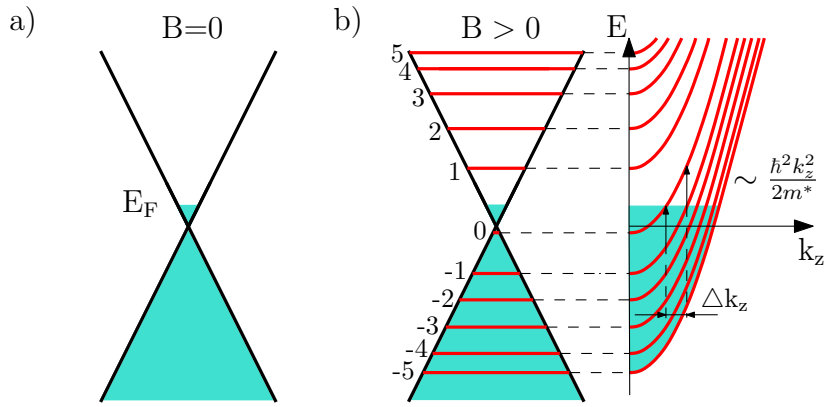

Fig. 3.4: The sketch of the band structure in the vicinity of the crossing point of the conduction bands a) at zero magnetic field and b) in the magnetic field with the dispersion of the LLs along the z direction.

4 PREPARATION OF SPECIMENS

As mentioned in Sec. 1, the thickness of the sample plays a major role in observing the inter-Landau level transitions. One can even say that a proper sample preparation is one of the most important parts of our experiment. Usually, cutting thin samples out of a bulk piece of the material does not give us more information considering the transmission experiments. Simply put, there is nothing interesting to see within the sample transparency region. Moreover, below the plasma edge ω_p and above the effective bandgap[1] $E_\mathrm{g}^\mathrm{eff}$ everything is suppressed by the strong absorption and the self standing sample is totally opaque for any achievable thickness. In fact, a sample thickness below the order of hundreds of nanometers would be needed in order to have a measurable transmission. In contrast to conventional materials, RSS in BiTeX gives rise to a specific non-Drude like absorption which significantly suppresses transmission above the plasma frequency, see transitions α and β in Fig. 4.1. By preparing sufficiently thin samples, we can expand the transparency window down to the plasma frequency which will allow us, as shown later on, to perform LL optical spectroscopy of BiTeX systems.

4.1 Optical response at B = 0

Although the experiment in the reflection configuration has also been performed, mainly the transmission spectra are discussed within this thesis, because their interpretation is more straightforward. The qualitative sketch of the absorption and transmission in our sample at zero magnetic field is shown in the Fig. 4.1. The transmission is linked to the optical conductivity (absorption) via the following approximation:

$$T \approx 1 - \frac{\mathrm{Re}\,\sigma_{xx}}{\varepsilon_0 c}, \tag{4.1}$$

where $\mathrm{Re}\,\sigma_{xx}$ is the real part of the optical conductivity, c is the speed of the light and ε_0 is the vacuum permittivity.

A group of van der Marel from Geneve recently performed a study of BiTeBr and BiTeCl optical properties [8]. This paper summarizes optical properties including reflectance and transmission at $B = 0$. However, the studied samples were relatively thick, around 10 µm for BiTeCl and 15 µm for BiTeBr. Fig. 4.2 shows a comparison

[1] It was experimentally observed that for a degenerate n-type semiconductor the optical activation energy is greater than the bandgap. It is known as a Burstein-Moss shift and leads to enhancement of bandgap $E_\mathrm{g}^\mathrm{eff} = E_\mathrm{g} + (1 + m_\mathrm{e}/m_\mathrm{h})E_\mathrm{F}$, where E_g is the energy of bandgap, m_e and m_h are the effective electron and hole masses and E_F is the Fermi energy as measured from the bottom of the conduction band [39]. The effective bandgap is shown in Fig. 4.1 a) as γ energy.

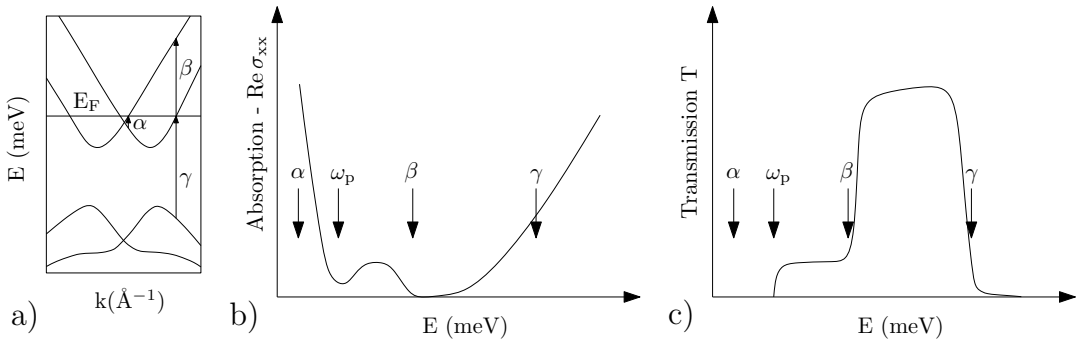

Fig. 4.1: Qualitative sketch of the a) transitions within the band structure, b) the absorption and c) the transmission spectra.

of the transmission through their 15 µm thick sample of BiTeBr and our 3 µm thick sample of the same material. This comparison proves that thickness of the sample matters, since we are able to see transmission in the $\alpha - \beta$ region, whereas authors of Ref. [8] are not. For thick samples, the non-Drude like absorption is too strong, therefore suppressing the transmission which is sensitive to the change in a magnetic field. For BiTeI and BiTeCl we get analogous behavior. The modulation in our spectra corresponds to the series of Fabry-Pérot interferences due to the monocrystalline nature of our sample, suggesting small deviations from parallelism of cleaving planes.

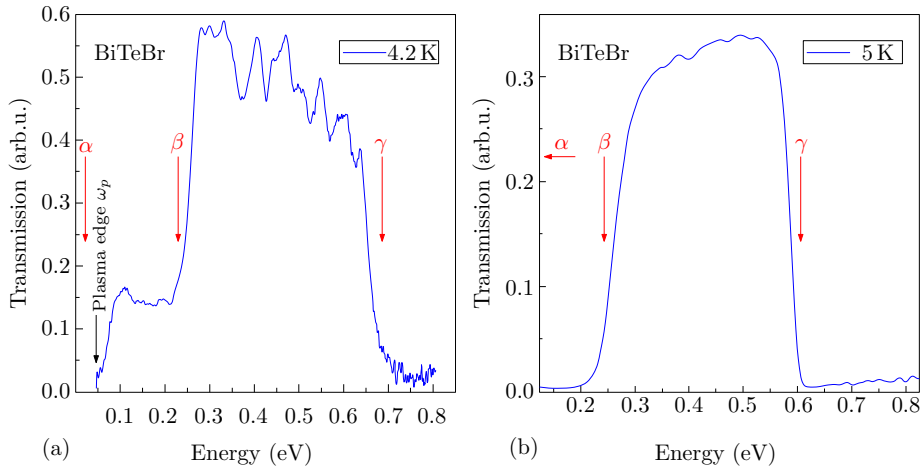

Fig. 4.2: (a) Comparison of our experimental data measured on 3 µm thick sample of the BiTeBr versus (b) experimental data measured on 15 µm thick sample of the BiTeBr which was reprinted from [8]. The temperature difference is negligible.

4.2 Mechanical cutting/cleaving

The bulk crystals of the BiTeX materials were prepared in Novosibirsk laboratories. Single crystals were grown from Bi-Te-I, Cl or Br melts using the Bridgman method. This Russian group has successfully prepared Bi_2Te_3 crystals with a natural p-n junction using a similar method [40]. One possible way to prepare thin samples out of a bulk piece of a material is to cleave them. In crystallography terms, cleavage is the tendency of crystals to split along certain crystallographic planes. Depending on their mode of crystallization, different types of cleavage exist. Since the BiTeX materials crystallize in hexagonal structure and consist of the continuously stacked atomic layers, they exhibit a basal cleavage along the horizontal xy plane (perpendicular to the c-axis) [41]. Crystals with basal cleavage can be peeled which is also case of the BiTeX materials. An example of the basal cleavage are the mica minerals.

4.2.1 Manual rotary microtome Leica

The rotary microtome Leica RM2125 TS, see Fig. 4.3, is a manually operated instrument which is designed for creating the thin samples of various thicknesses for use in routine and research laboratories. Notably, the main application of this instrument is sectioning of specimens embedded in the soft paraffin in biological laboratories. It is also possible to slice harder specimens as long as they are suitable for being

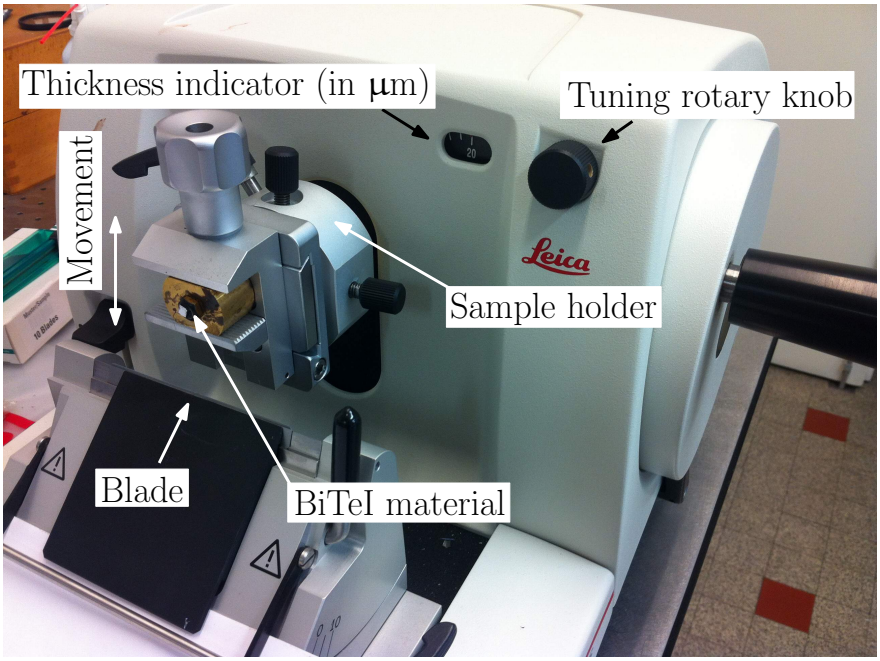

Fig. 4.3: Simple description of the rotary microtome Leica RM2125 TS which was used to prepare the samples.

mechanically cut. As the BiTeX materials are easy to peel, the manual rotary microtome is the perfect solution. Slicing is possible in a specific range of thickness: 0.5-60 μm. The desired thickness can be set via a rotary knob and accurately read from the thickness indicator. The mounted sample can be oriented in both vertical and horizontal directions as well as rotated by an angle of $\pm 90°$ [42].

4.2.2 Typical samples prepared

The samples were prepared out of the bulk crystals of the BiTeX materials. The bulk crystal was fixed on a specially designed brass holder using a sealing-wax as shown in Fig. 4.3. The next step was inserting the brass holder into the sample holder and rough positioning of the sample parallely to the blade. This was done using a horizontally adjusted laser in such a way that the reflected beam out of the sample surface should follow exactly the same optical path as the incident beam. After the positioning, several initial cuts have to be performed to flatten the sample surface. Usually, the high section thickness is used, e.g., 10 μm. At this point, we have a suitable smooth surface ready to be sliced. At the beginning, the section thickness around 5 μm is used and several samples are prepared. The section thickness is subsequently reduced and a new set of thinner samples is prepared. This process is repeated until the samples with the lowest possible thickness are prepared. Depending on the quality of the material, there is a limiting thickness below which the material starts to fall apart during the slicing[2]. The size of the sliced samples should be sufficiently larger in order to be manipulated. Very often the samples were rolled after slicing as shown in Fig. 4.4 b) and we had to unroll them without causing any damage. For this purpose the tweezers and wooden toothpicks were used. Rigid metallic tapes with holes in their centers were prepared in advance. This tape is sticky on one side; therefore, it holds the sample and avoids unnecessary bending or mechanical damaging. The sliced film of material was placed over the hole with approximately 1 mm in diameter and very carefully unrolled over this hole using a wooden toothpick.

It is necessary to make sure that the sample is well-positioned and there is no light leak around the edge of the hole or even through the sample itself[3]. It may happen that the sample and hole are misaligned or the sample was damaged or punctured during the positioning. This unfortunately means that the sample is irreversibly damaged and another one has to be prepared. However, for the experienced and

[2]The smallest achieved thickness was 0.5 μm for the BiTeI material. Nevertheless, there is always a slight deviation. To verify real thickness, the profilometry would be needed.

[3]The easiest way how to check the presence of a leak is to hold the tape with the sample in front of the lamp and look through the hole.

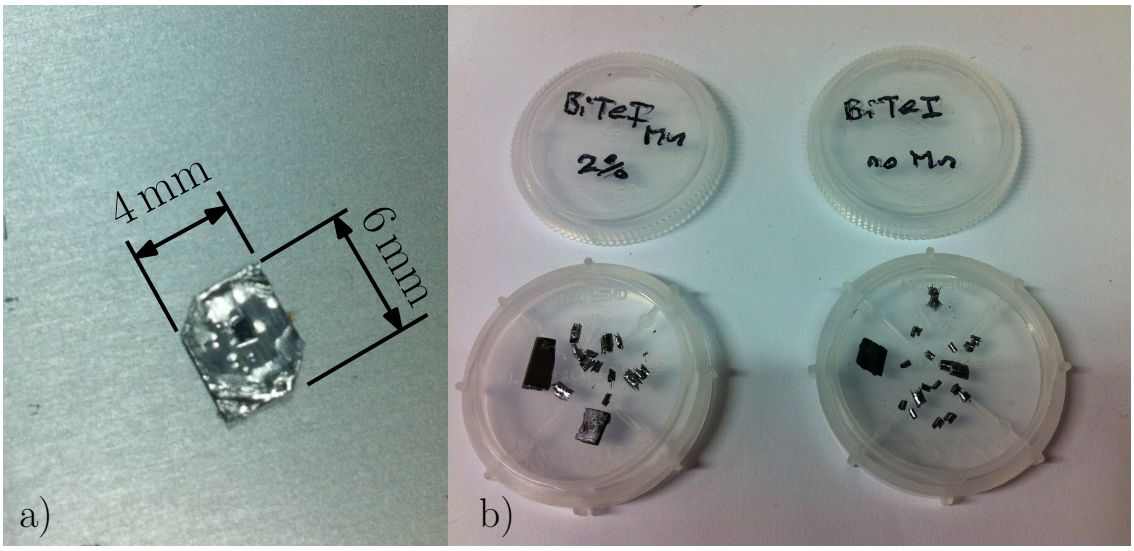

Fig. 4.4: Photo of the a) final appearence of the sample on the metallic tape and b) the sliced films of the material - note the rolled pieces.

skilled worker the success rate is 7 good samples out of 10. The sample on the metallic tape in its final appearance can be seen in Fig. 4.4 a).

4.3 Exfoliation

To reduce the sample thickness further, exfoliation is another natural possibility. The exfoliation as the method of the samples preparation is widely known in particular from graphene. Among the first pioneers of the mechanical exfoliation we have to include Geim and Novoselov. They prepared thin films of graphene out of pyrolitic graphite by simple repeated peeling [43]. Since the BiTeX materials are easy to peel-off, the exfoliation can be performed.

4.3.1 Process of sample exfoliation

There are different types of exfoliation techniques; in this case, we have used the one containing wet processes. The right equipment is a key element for a successful exfoliation and following transfer onto the silicon substrate with an aluminum mask. For this reason, the adhesive tape of medium adhesion strength (Microworld F07xx) [44] and WF film (Gel-Pak X4) [45] were used to improve the quality of the exfoliation process. A bulk piece of material is placed on the adhesive tape, pressure is applied for a few of seconds and then taken away. If the amount of material left on the adhesive tape is sufficient, exfoliation is performed repeatedly by sticking two parts of the tape together. In the next step, adhesive tape is sticked to the WF film

and moderately pressed for about 30 s. Afterwards, it should be encumbered using a small weight for about 5 minutes. Finally, the adhesive tape has to be rapidly detached from the WF film.

In the meantime the Si substrates were prepared - deposition of the alignment markers and spincoating of the LOR 3A resist at speed of 7000 rpm for 45 s, including baking for 5 min at 150 °C. Thus prepared Si substrates covered by the resist are used as target substrates for another flake transfer. The WF film and substrate were brought into contact and as previously mentioned, pressed against each other for about 30 s. This time, the WF film and substrate are encumbered for about 10 min. Detachment of the WF film from the substrate is the most crucial part concerning the amount of transferred material. A quick detachment will remove a larger amount of the material residing on the substrate whereas slower peeling-off provides more accurate control over the quantity and thickness of the flakes. Therefore, the detachment should be very slow, specifically 2 cm per minute. Results of the transfer can be reviewed by using the optical microscope where the size of the flakes can be determined, as shown in Fig. 4.5. One should also note the position of the promising flakes with respect to the alignment markers. At the end the second layer of the resist is spincoated over the flakes, note green colour in Fig. 4.5 a) - 4% PMMA spincoated at speed of 4000 rpm for 45 s, including baking for 3 min at 150 °C.

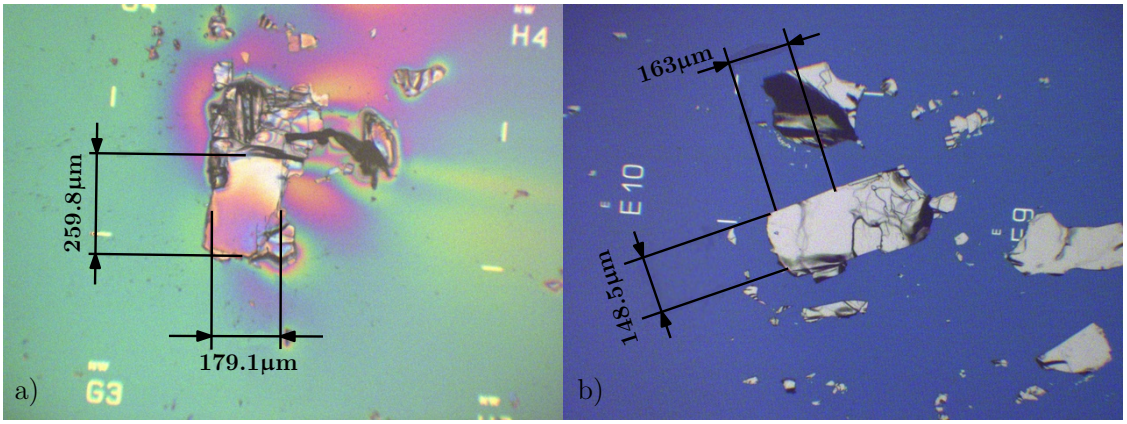

Fig. 4.5: Photo of a) the flake sandwiched between LOR 3A and 4% PMMA resists and b) the flake on top of the LOR 3A resist.

4.3.2 Typical samples prepared

For the transmission measurements, specific substrates with the aluminum mask consisting of approximately 110 nm-thick continuous layer of aluminum with a hole in its center had to be used. The purpose of the hole is to allow light pass through the

substrate whereas everywhere else the light is reflected. There were three different hole diameters, i.e., 100, 150 and 200 µm. Substrates have a size of $3 \times 3\,\mathrm{mm}^2$. Due to the alignment markers, finding the chosen flakes was much easier. Special tape windows were prepared out of ICROS$^{\mathrm{TM}}$ tape which is usually used to protect silicon wafers [46]. These tape windows had outer dimensions $10 \times 10\,\mathrm{mm}^2$ and inner dimensions $5 \times 5\,\mathrm{mm}^2$. Tape windows were placed on the target substrate with the flakes using the optical microscope in such a way that each flake was in the center of the tape window. Then, resists were scratched along the outer edge of the tape window using a sharp tip, as shown in Fig. 4.6 a) Step 1. Subsequently, the substrate was inserted into the beaker with a LOR 3A dissolvent MF26A. The tape window with a film of PMMA resist holding the flake on the bottom side was floating on the surface within a few minutes. The next step is a bit tricky: the flake has to be precisely aligned with the hole in the aluminum mask, see Fig. 4.6 a) Step 2. For this task, we used conventional UV photolithography mask aligner with eyepieces. When aligned, the substrate was slowly and carefully brought into contact with the flake. Now, the hole is completely covered by the flake. The very last step was to scratch the PMMA resist along the inner edge of the tape window which can be seen in Fig. 4.6 a) Step 3, and dissolving the PMMA in acetone. Eventually, additional cleaning in the oxygen plasma can be performed. Figure 4.6 b) shows finished samples which were inserted into the probe inside the cryostat and magneto-spectroscopic measurements were performed. Although the flakes were undoubtedly thinner, the transmission signal was very weak as compared to the sliced samples. By chance, we may have found a compromise between the thickness and size of the sample surface.

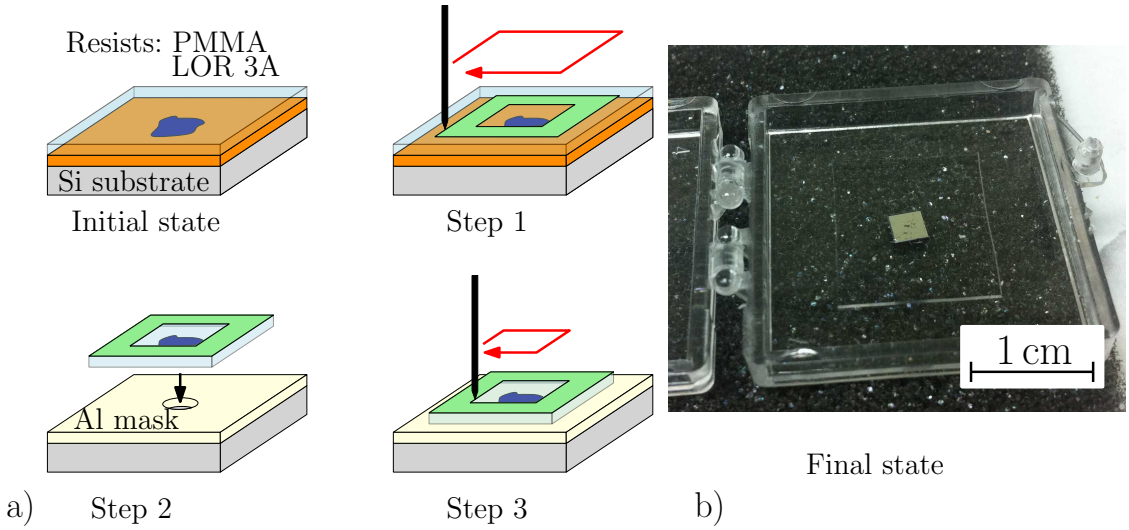

Fig. 4.6: a) Process of the flake transfer from the target substrate onto the substrate with the aluminum mask. b) Photo of the finished sample.

4.3.3 Possible modifications

One of the eligible approaches of how to increase the transmission signal is to decrease the thickness of the flakes even more, up to one atomic layer. Nevertheless, we tried rather easier solution. There is a Winston cone at the end of the probe (more detailed description of the experimental setup will follow in next section) which is a non-imaging light collector in the shape of an off-axis parabola with a reflective inner surface. Our goal was to design the Winston cone in such a way that light would be better focused on the tiny flake - a smaller output aperture diameter. Also the sample itself was moved as close to the detector as possible to hinder light scattering underneath the sample, see Fig. 4.7. This modification will be tested and possibly further upgraded. Extensive experiments exploring the exfoliated samples will be performed in the future, therefore within this thesis we present only experimental data measured on the sliced samples.

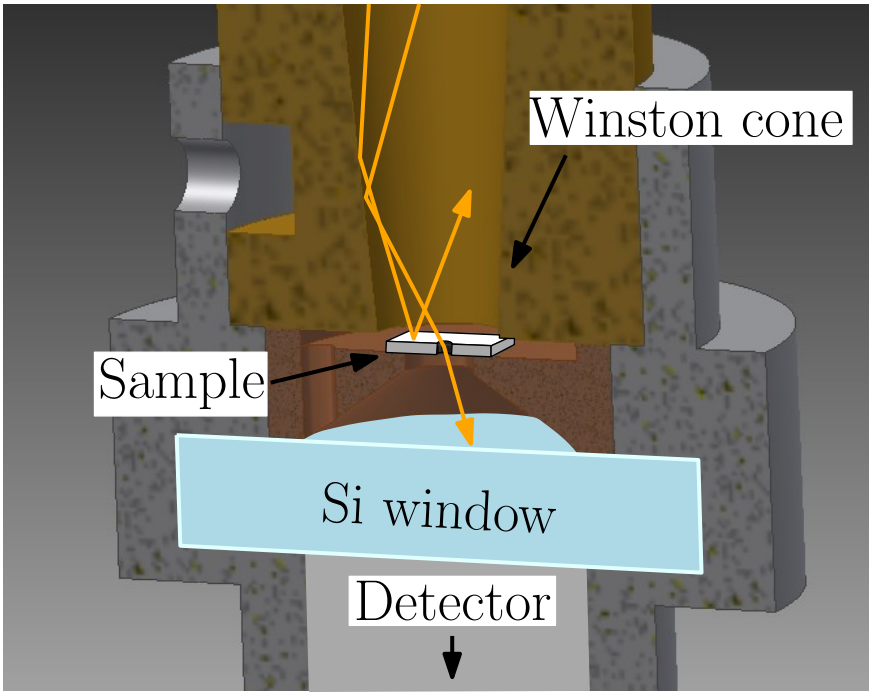

Fig. 4.7: A 3D model of the designed Winston cone with the sample on the centering/spacer ring.

5 EXPERIMENTS

As mentioned in Sec. 4.1, our measurements were performed in two configurations: in transmission and in reflection. Figure 5.1 a) shows a simple scheme of the transmission configuration. Figure 5.1 b) shows the scheme of the reflection configuration where a beamsplitter is included and a detector is located outside the magnet. However, the reflection measurements were more complicated with respect to a setup alignment and noise elimination. Moreover, interpretation of the experimental data measured in reflection configuration is more difficult as compared to the transmission configuration. Hence, only transmission measurements have been performed and this thesis summarizes our findings. If interested in reflectivity measurements, we may refer readers to, e.g., Dr. Bordác's work [7].

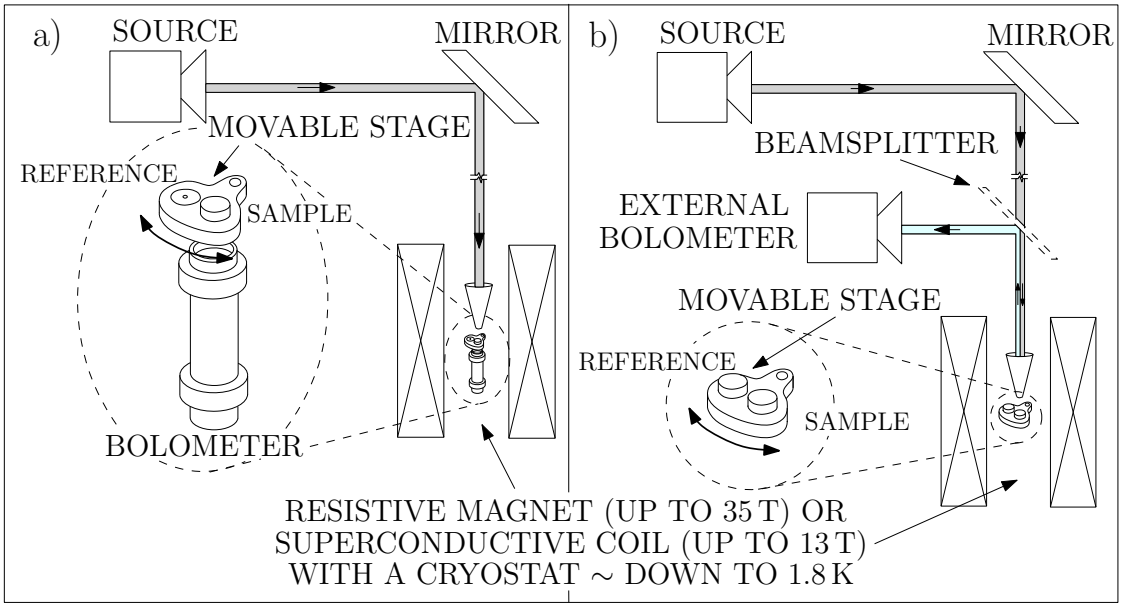

Fig. 5.1: Simple schemes of the a) transmission configuration and b) the reflection configuration.

5.1 Low-field measurements - superconductive coil

In the IR laboratory in LNCMI Grenoble, there is a superconductive coil which provides field of up to 13 T when cooled down to 1.8 K. This coil is mainly used for long-standing measurements within its field range and as in our case for a quick characterization of our samples. Since the operating costs are adequate, one can take the time to choose only the best samples for the high-field measurements.

5.1.1 Experimental setup

The main component of our experimental setup is undoubtedly the Fourier Transform Infrared (FT-IR) spectrometer *Bruker Optics - IFS 66v/S*, whose spectral range varies from far-IR (FIR) to the near-UV. The desired spectral range can be set by the choice of the beamsplitter (T222 - multilayer mylar, KBr, etc.) and the radiation source (Hg lamp, Globar, etc.). Since this is the interference spectrometer, a gas supply for air bearings (movable mirror) is required. We use a gaseous nitrogen from a self-pressuring Dewar flask. The sample is glued onto one side of the movable stage, whereas on the other side is the reference (1 mm diameter aperture). This stage is at the end of the inner component of the probe. Then a bolometer is placed below this stage and connected to the wires leading outside to the male jaeger connector. When everything is connected, tightened and the movable stage can freely rotate, the inner component is inserted into the probe - stainless steel tube. Afterwards, the free end of the probe, where the light enters, is covered by a window (ZnSe, Si, etc.) in order to be able to pump out the air from the probe. This is important for enabling the free space propagation of light. It is good to let the probe pump out for at least half an hour. Once the probe is pumped out, the valve is closed and cooling the probe down may start. The probe is inserted into the cryostat full of liquid helium. Cooling the probe down usually takes 15-20 min. Inside the cryostat, there is a superconductive coil made of Nb_3Sn which provides field of 11 T at 4.2 K and 13 T at 2.2 K. The radiation from the spectrometer is guided into the probe via a custom-made box with a golden-plated parabolic mirror. This mirror sits on the three screws and therefore its position can be changed in order to gain signal at the bolometer. The bolometer is coupled back to the spectrometer via a female-male jaeger (plus a preamplifier) connection. To help the reader to imagine the above described experimental setup, Fig. 5.2 is provided. The transmission signal is processed and the provided software (OPUS) displays an interferogram which can be further transferred into the transmission spectra.

5.1.2 Experimental data

Examples of the transmission spectra measured at low fields are shown in the following figures. Those are raw data, some not corrected for the field induced changes in response of the bolometer which is demonstrated by a slope of the spectra. To correct this response, a reference has to be measured separately by probing a free aperture (hole) in the movable stage. For example, Fig. 5.3 directly shows the non-corrected transmission spectra of BiTeI. In other words, what we see are the spectra showing the relative change of transmission with respect to the transmission at zero field. Another phenomenon, which we have often observed, are series

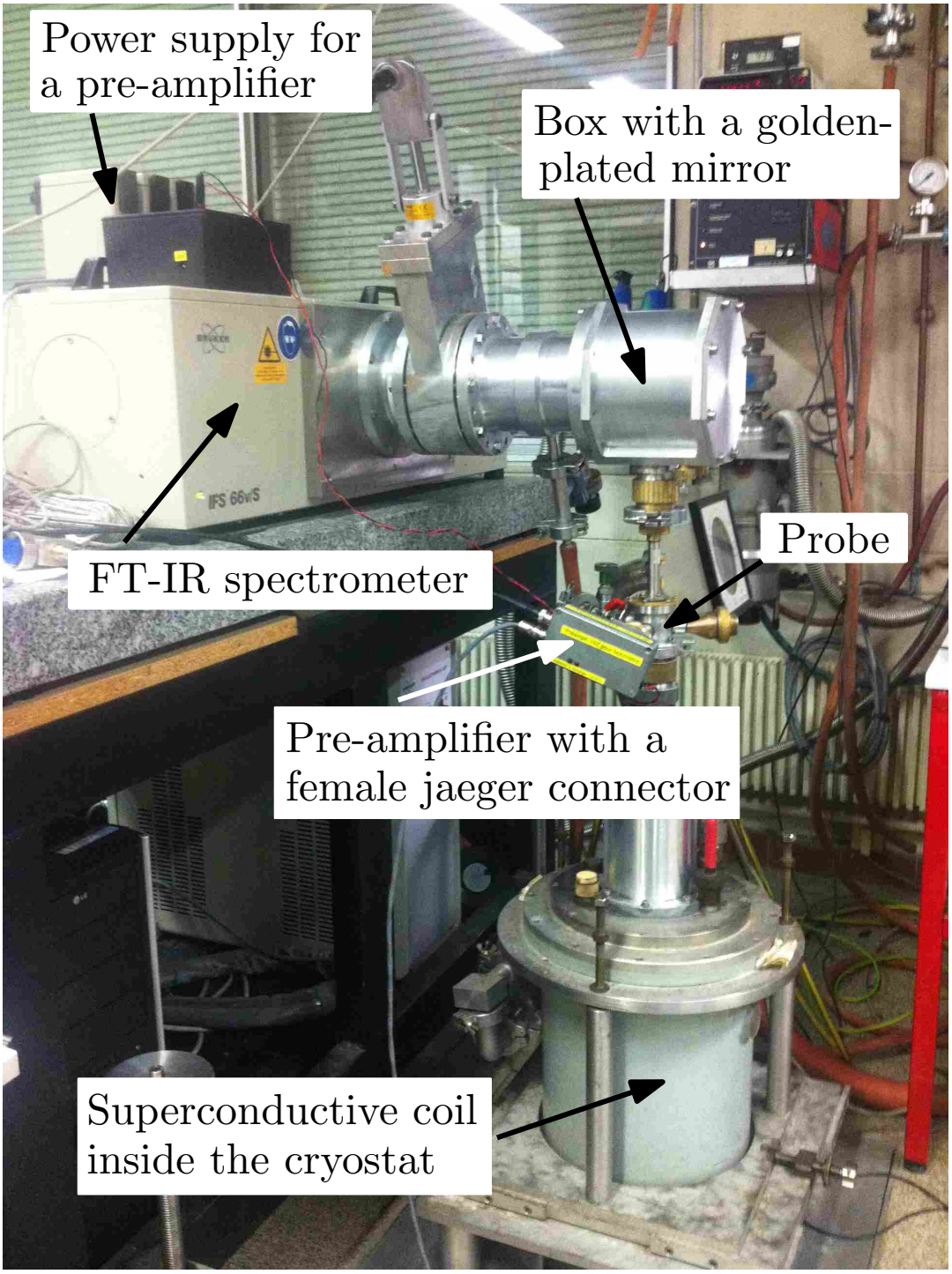

Fig. 5.2: The experimental setup for low-field measurements.

of Fabry-Pérot interferences, as seen in Fig. 5.4. This interference may occur when the sample is almost an ideal plan-parallel slab. There is a considerable probability that during the sample preparation we cleave plan-parallel film of material instead of ordinary slicing, particularly when the BiTeX materials are easy to peel materials. The last graph in Fig. 5.5 shows a prime example of the BiTeBr transmission spectra measured up to 13 T.

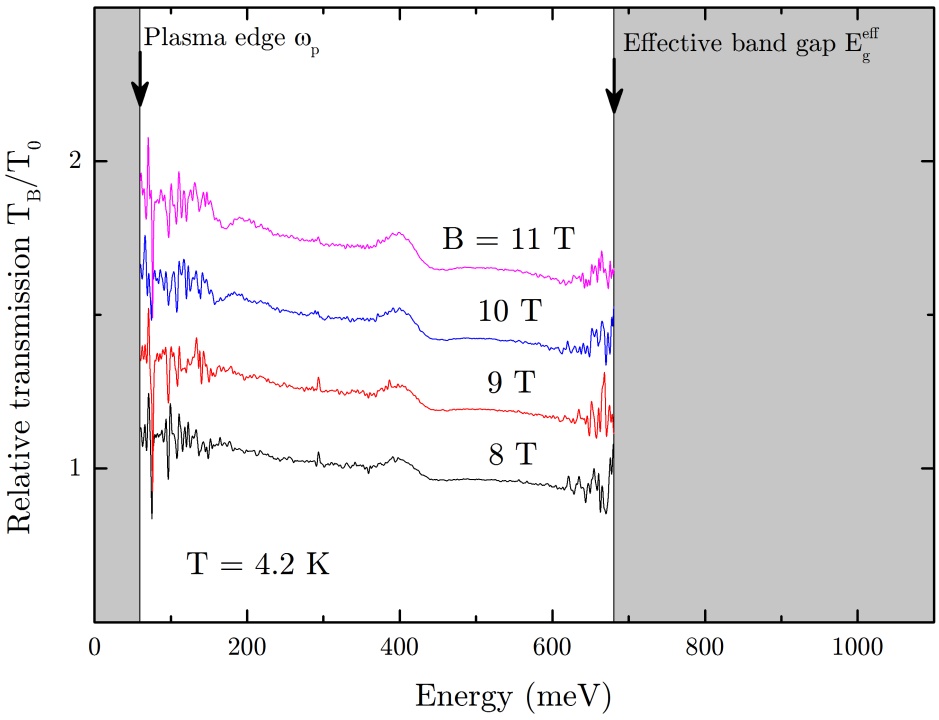

Fig. 5.3: The relative transmission spectra of BiTeI measured without reference causing the slope, which is the bolometer response.

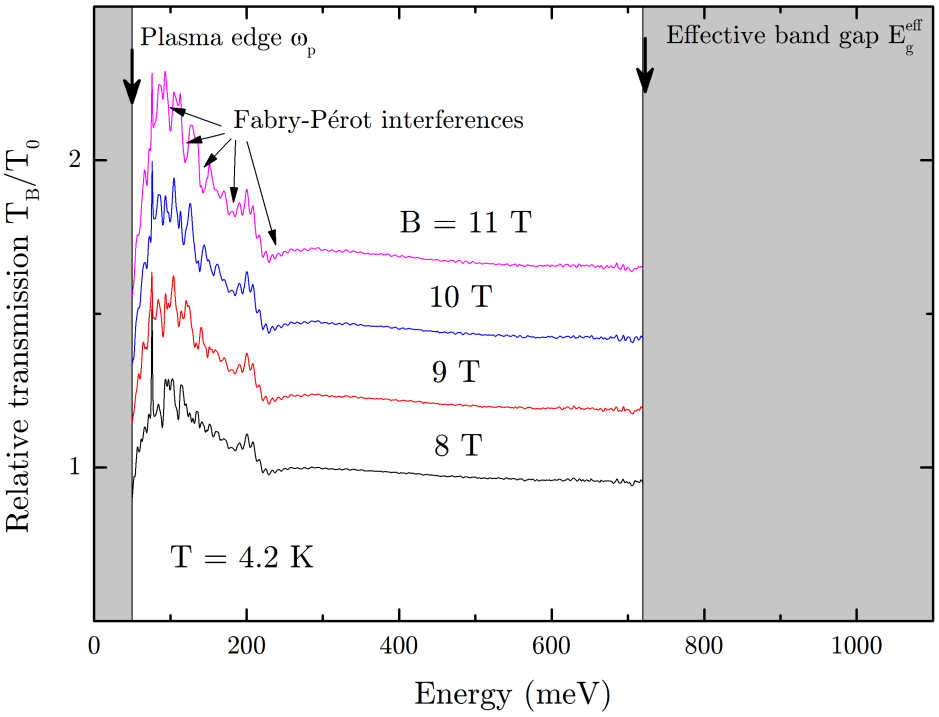

Fig. 5.4: The relative transmission spectra of BiTeCl, which is diametrically different from the two remaining spectra. Note the series of Fabry-Pérot interferences.

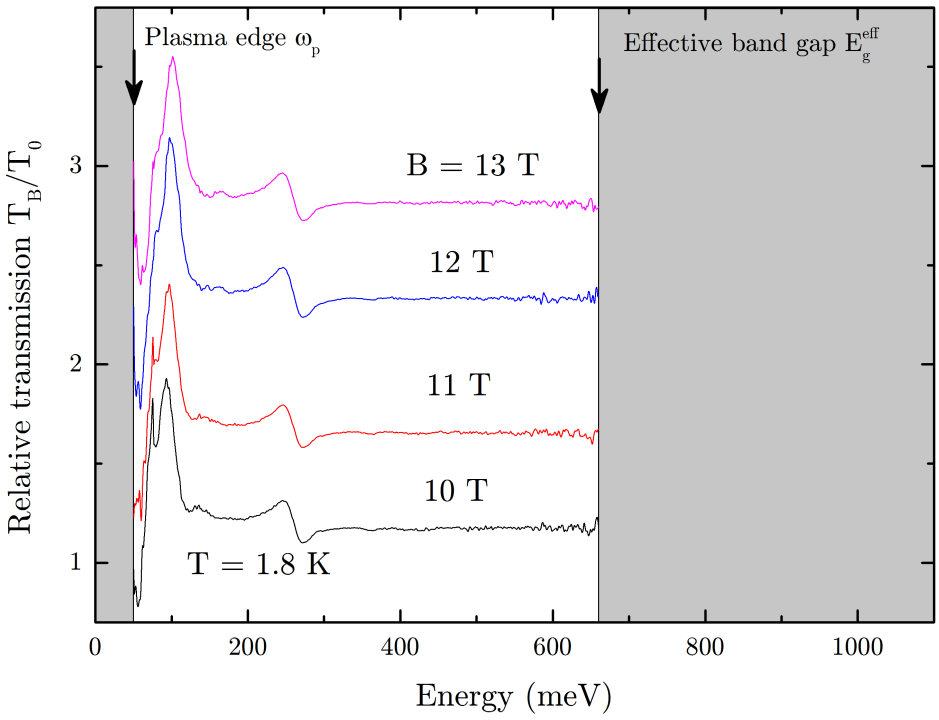

Fig. 5.5: The relative transmission spectra of BiTeBr measured up to 13 T at 1.8 K.

5.2 High-field measurements - resistive coil

As soon as we have chosen all the best samples worth being examined, we can start to prepare an experimental setup for the high-field measurements. In comparison with the superconductive coil, a resistive coil has a much higher operating cost. Therefore, everything should be prepared in advance in order to not waste the time. Every user has a limited amount of "magnet"time designated for his/her experiments. Experimental groups work in day or night shifts, since two high-power magnets cannot operate at the same time. Our interest will be focused only on a M9 resistive magnet[1] because the most high-field experimental data were measured using this particular magnet.

5.2.1 Experimental setup

The experimental setup is analogous to that used at low fields, except for the fact that it is coupled to the resistive magnet in the high-field installation of LNCMI. By using the resistive magnet, much higher fields can be reached and there comes a danger of a so-called *missile effect*. All the magnetic objects should be secured and in the safe distance from the magnet. Otherwise, they can be attracted to the

[1]M1, M5, M7, M8, M9 and M10 are an internal magnet notations within the LNCMI-G laboratory.

magnet and may cause serious damage, for instance: the puncture of the cryostat. For this reason, an oversized waveguide is used to transfer the light from the FT-IR spectrometer to the probe, so the equipment can be placed sufficiently far from the magnet. This waveguide is 2 m long and has an inner diameter of 150 mm. At the end of this waveguide, there is also located the same custom-made box with a golden-plated mirror. The M9 resistive magnet is situated in the basement under the floor and consists of 14 helices[2]. It provides a magnetic field of up to 36 T using the full power supplied by the 24 MW installation and has an internal diameter of 34 mm. The cryostat is a separate component and has a long tail which fits into the magnet bore. Coils are supplied by a DC current (up to 30 000 A) and cooled by a demineralised water with a flow rate of 300 l/s in a closed loop [48]. Hand in hand with this performance comes the problem of vibrations due to flowing water which decreases signal-to-noise ratio in our data, see Fig. 5.7. Thus, the only parameter we can influence is a position of the cryostat tail inside the bore of magnet.

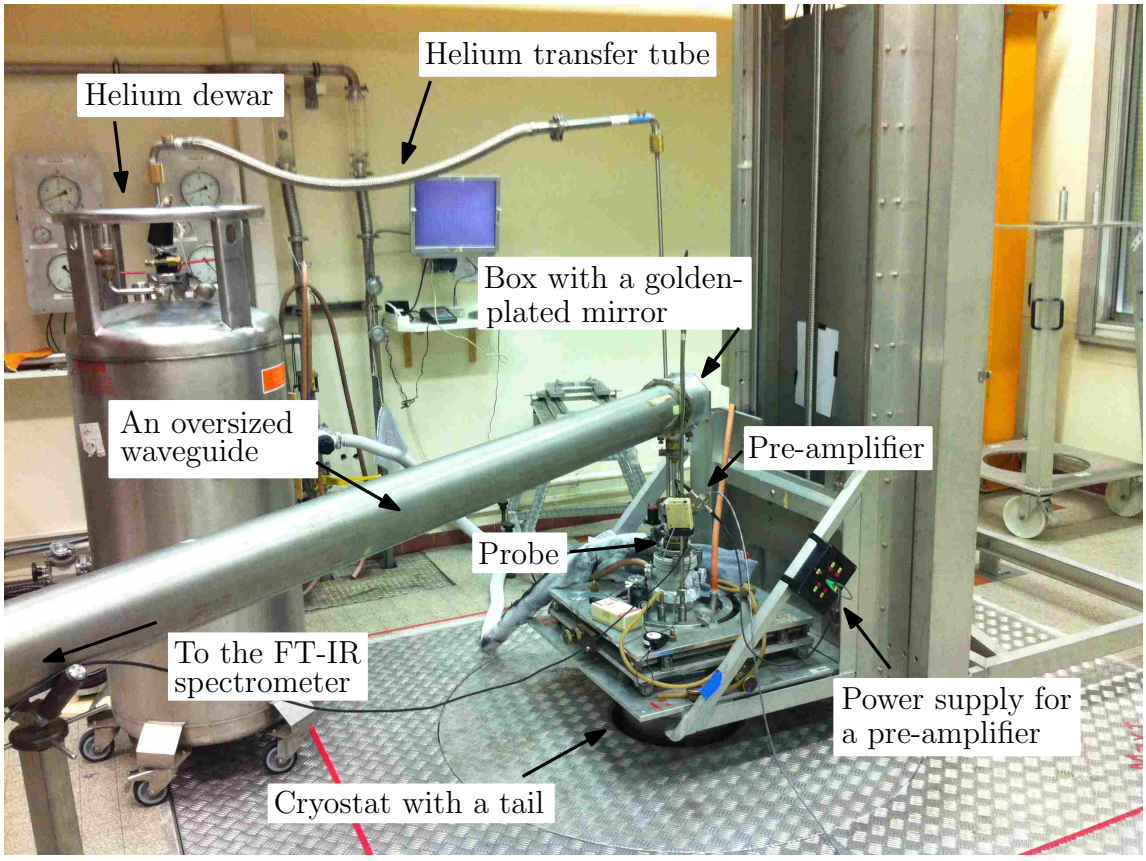

Fig. 5.6: The experimental setup for high-field measurements.

[2]The word *helix* comes from the Greek word meaning 'twisted' or 'curved'. Mathematically, the helix is a type of smooth space curve. Its special property is that the tangent line at any point makes a constant angle with an axis [47].

This tail has to be in the center and should not touch the walls of the bore. To have a better notion of this setup, Fig. 5.6 is provided.

5.2.2 Experimental data

Examples of the transmission spectra measured at high fields are plotted in the following figures. The high-field transmission spectra provide a deeper insight into the effects induced by the magnetic field. For instance, Fig. 5.7 shows relative transmission spectra with the dips at low energies which clearly evolve with the magnetic field. Also the reader should note that the level of noise has increased and this fact may cause problems during the interpretation of the experimental data. If we compare Fig. 5.4 and Fig. 5.8, we conclude that only the intensity at low energies highly increases. The shape of the spectra itself also suggests that BiTeCl is not an ordinary family member of the BiTeX materials and it is probably related to the topological nature of BiTeCl material. On the other hand, Fig. 5.9 shows again already known data; however, slightly different as compared to the BiTeI material. The BiTeBr material was measured only up to 29 T due to the assignment of another magnet, i.e., M10 during the second round of high-field measurements in October 2014.

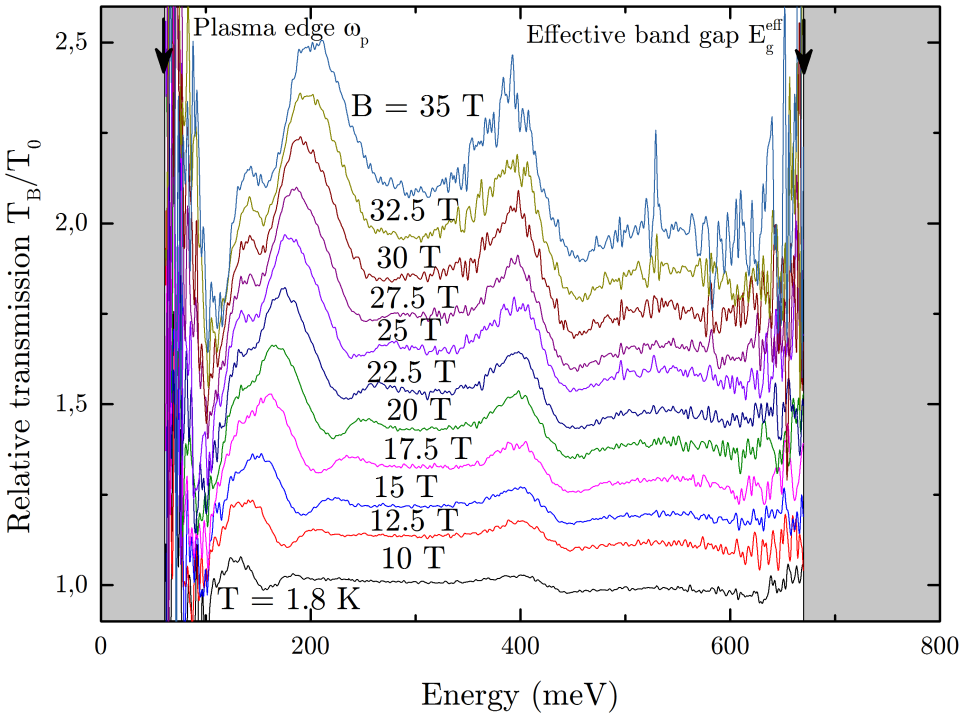

Fig. 5.7: The relative transmission spectra of BiTeI measured up to 35 T. The noise at higher fields originates in the vibrations of the magnet due to flowing cooling water.

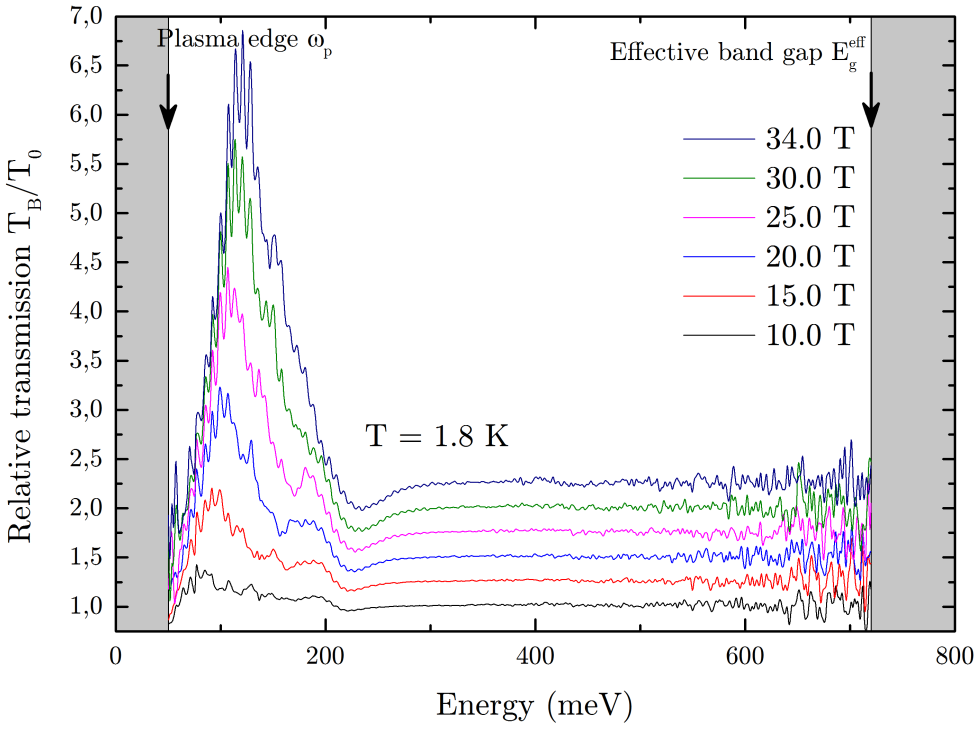

Fig. 5.8: The relative transmission spectra of BiTeCl at high fields. Note the very high increase in intensity at low energies.

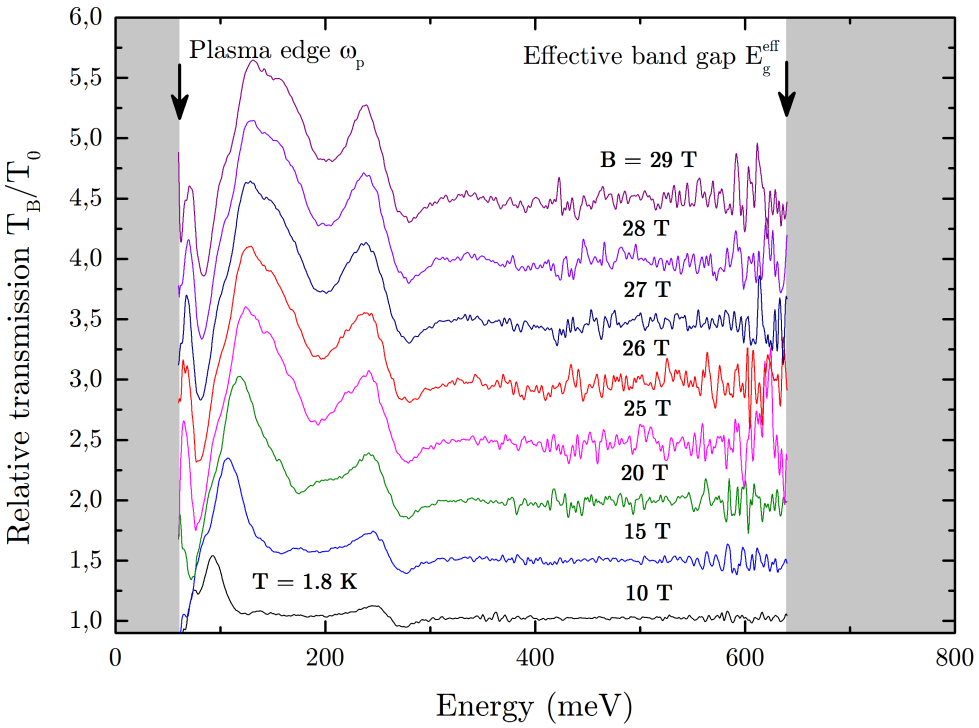

Fig. 5.9: The relative transmission spectra of BiTeBr measured up to 29 T at M10.

5.3 Magneto-transport measurements

Magneto-transport measurements as a complementary technique were performed at the Institute of Physics of Materials of the Academy of Sciences of the Czech Republic (IPM ASCR) in Brno. The experimental setup for the electric transport measurements at low temperature in the magnetic field is located there. Main objective of this measurement is a study of the Shubnikov-de Haas (SdH) oscillations in BiTeX compounds where the large RSS enables the separation of the SdH oscillations with respect to their origin either from the inner (IFS) or the outer (OFS) Fermi surface as observed, e.g., in Ref. [49]. The frequencies of the SdH oscillations provide us with information about the extremal Fermi surfaces areas and their temperature dependence allows us to estimate the corresponding cyclotron masses as shown, for instance, in Ref. [50].

Naturally, the exfoliation was considered to be the best way to prepare a specimen for transport measurements. We prepared several specimens by mechanical exfoliation of the BiTeX bulk crystals; however, it should be noted that only samples of BiTeBr were measured so far. The flakes of the material were subsequently contacted via two golden connections which were manufactured by means of the electron beam lithography. The initial measurements have revealed the resistance in order of MΩ, suggesting problems with high resistance at the flake-golden contact interface. Therefore, we have decided to perform test measurements on a macroscopic scale. A thin piece of the bulk crystal was cleaved and contacted by the silver paste, see Fig. 5.10 a). This two terminal method provided us with the field-dependence of the resistance plotted in Fig. 5.11 a) which indicates clear signs of quantum oscillations (the black arrows). Nevertheless, further analysis is complicated by not well defined

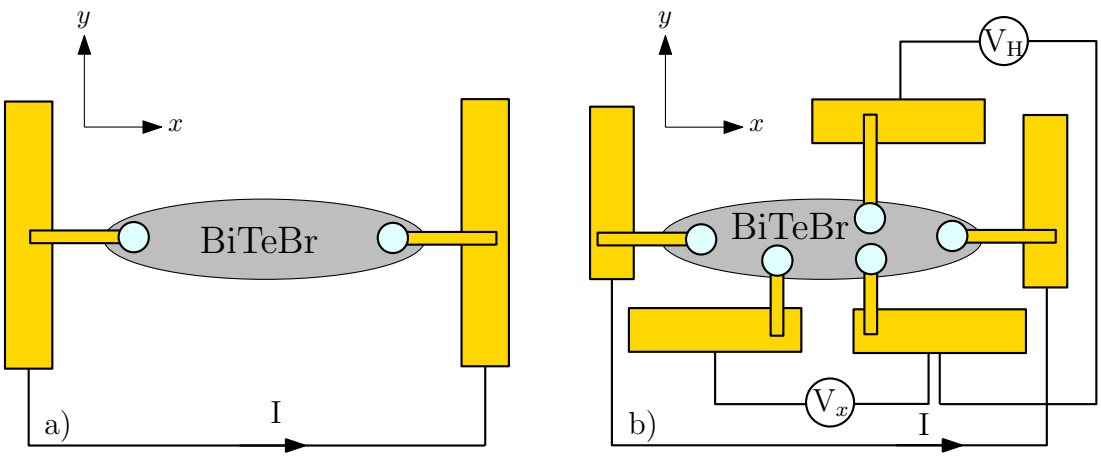

Fig. 5.10: The scheme of a) the two terminal method for the resistance measurements and b) the five terminal method for the ρ_{xx} and ρ_{xy} components measurement.

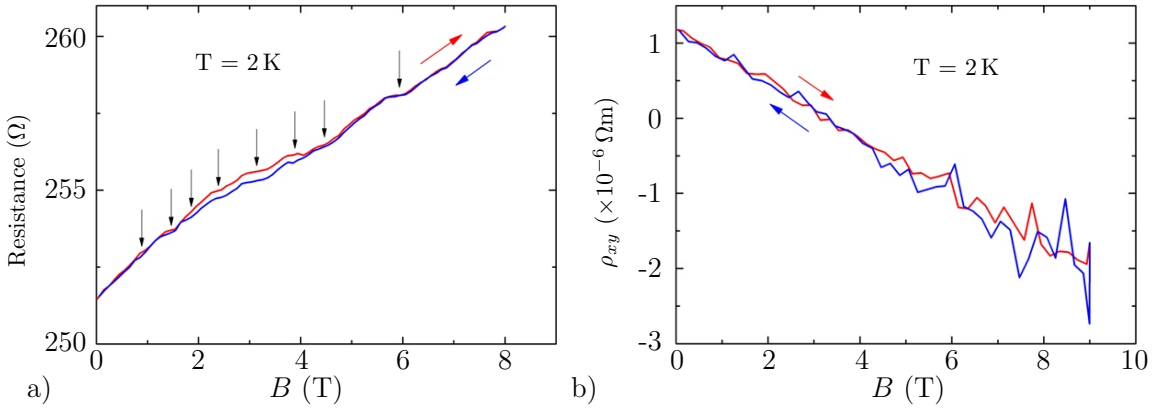

Fig. 5.11: a) The dependence of the resistance on a magnetic field measured by two terminal method on BiTeBr sample, where the black arrows indicate possible plateaus in the resistance. b) The dependence of the transverse component ρ_{xy} on a magnetic field measured by five terminal method on BiTeBr sample. In both graphs the red arrow indicates sweep up to 8 T (9 T respectively) and the blue arrow sweep down to 0 T.

geometry of electrical contacts which mixes contributions of the longitudinal R_{xx} and transverse R_{xy} resistances. To measure separately both components, we added three more contacts, see Fig. 5.10 b). This five terminal method was also realized on a macroscopic sample when a small piece of bulk crystal was contacted using silver paste. Unfortunately, no signs of quantum oscillations have been observed in the ρ_{xx} signal and further analysis was impossible. The unexpected decline of resistance with the applied magnetic field was assigned to the contact effects. This suggests that contacts should be manufactured properly by the e-beam lithography in a Hall bar geometry which is widely used for magneto-transport measurements. On the other hand, the transverse (the Hall resistivity) component ρ_{xy}, see Fig. 5.11 b), exhibits right the same behavior as seen for example in Supplementary Materials of Ref. [49]. In fact, the negative slope of the ρ_{xy} suggests that the charge carriers are electrons [49]. A simple linear fit implies the carrier density $n \approx 2 \pm 1 \times 10^{19}\,\mathrm{cm}^{-3}$ calculated using standard Hall effect formula:

$$\rho_{xy} = \frac{V_\mathrm{H} t}{I} = -\frac{1}{ne} B, \tag{5.1}$$

where the V_H is the Hall voltage, I is the current, $t = 0.1\,\mathrm{mm}$ is the thickness of the material. The deduced electron density is consistent with densities typical for as grown BiTeX specimens, see e.g. Refs [49] and [51]. In conclusion, the Hall measurements are more prone to errors, as the precise thickness where the current flows is difficult to know precisely.

6 QUALITATIVE COMPARISON OF THE EXPERIMENTAL DATA WITH RASHBA MODEL

We performed extensive magneto-spectroscopic measurements and explored a series of BiTeX specimens in the transmission configuration. Taking into account both low-field and high-field measurements, we have relevant sets of transmission spectra covering a wide range of magnetic fields for all BiTeX materials. The data taken on BiTeCl suffer from a relatively lower electronic quality of studied material and the high-field measurements on BiTeBr were performed later on (in late autumn 2014). Therefore in this thesis, we mainly focus on the most complete results obtained on BiTeI. The set of BiTeI transmission spectra goes from low-fields up to 35 T, thus giving the rich information from the perspective of magnetic field-induced features and their evolution. Characteristic high-field magneto-transmission data obtained on this material (BiTeI) are presented in Fig. 6.1 d). The relative magneto-transmission spectra exhibit two main spectral regions: highlighted in pink and yellow in which a specific magnetic-field-induced response is observed.

6.1 Spectral regions of interest

Let us now discuss the origin of these two spectral regions in Fig. 6.1 d). Pink-highlighted region at relatively low energies from the plasma edge up to about 250 meV and second yellow-highlighted one around the photon energy of 400 meV. The low-energy region corresponds to optical transitions in the the vicinity of the Dirac cone formed within the conduction band of BiTeI, see Fig. 6.1 a) and b). With the increasing magnetic field, a series of well-defined transitions develops, denoted in Fig. 6.1 d) by vertical arrows. These are inter-Landau level resonances and may be identified using previously published low-field data, see Ref. [7] and Fig. 6.1 b). Notably, these resonances follow nearly a $\sqrt{B}$ dependence, see Fig. 6.2, typical of Landau levels in systems with massless relativistic particles. The colored circles indicate a set of energies which was read out of the Fig. 5.7. The deduced positions of individual observed inter-Landau level transitions has been plotted into the fan chart in Fig. 6.2, together with an additional set of data kindly provided by Dr. Sandor Bordács (from another high-field experiment performed in LNCMI on samples from the group of Prof. Tokura, University of Tokyo). The size of symbols corresponds to the estimated experimental error given by the width of transitions and at higher magnetic fields also by noise in our spectra induced by the resistive magnet vibrations.

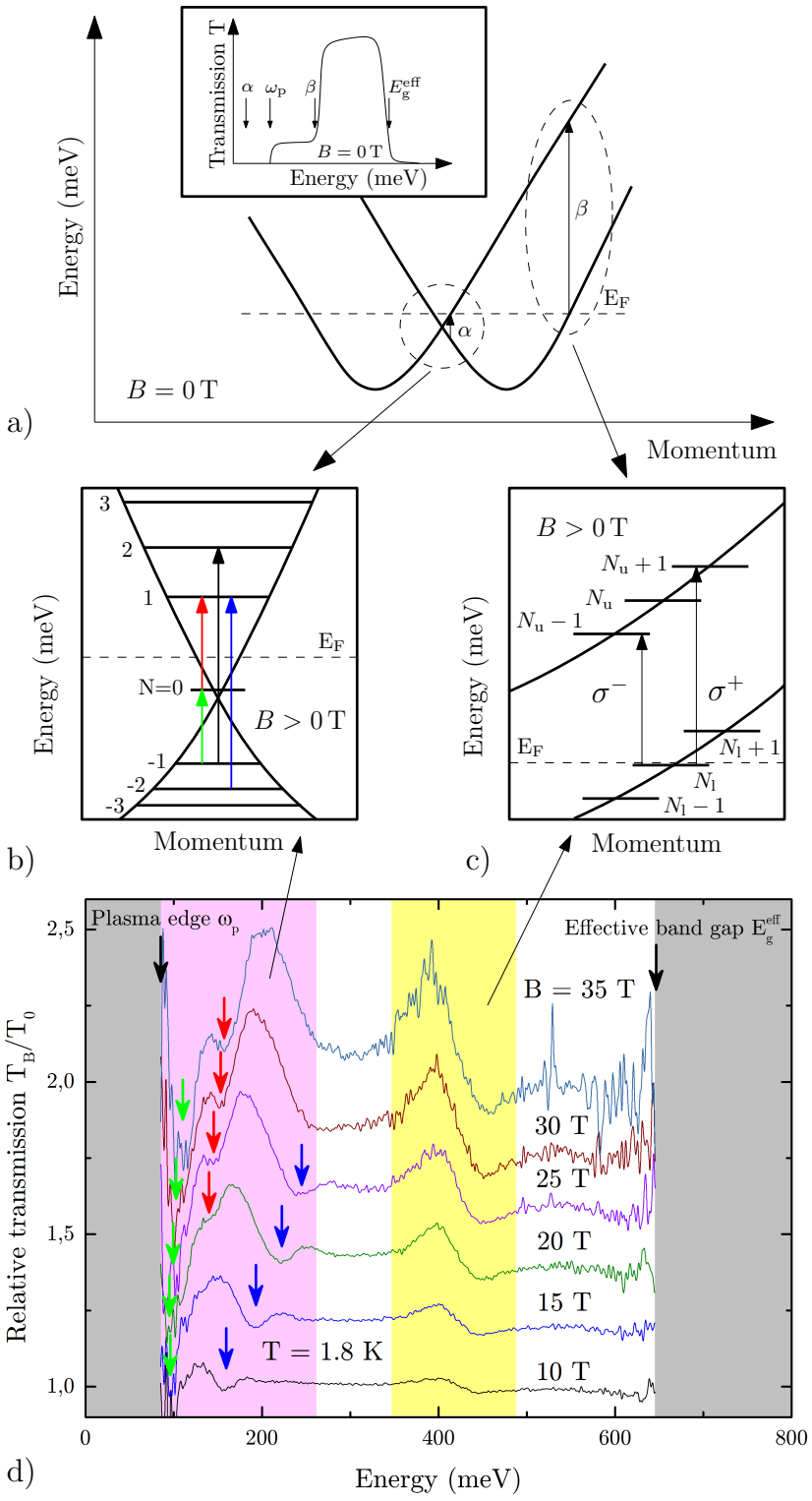

Fig. 6.1: a) The scheme of the conduction bands with two main regions defined b) by the α transitions related to the inter-Landau level transitions in the vicinity of the Dirac cone and c) the β transitions. d) The selection of the relative transmission spectra with highlighted spectral regions of interest.

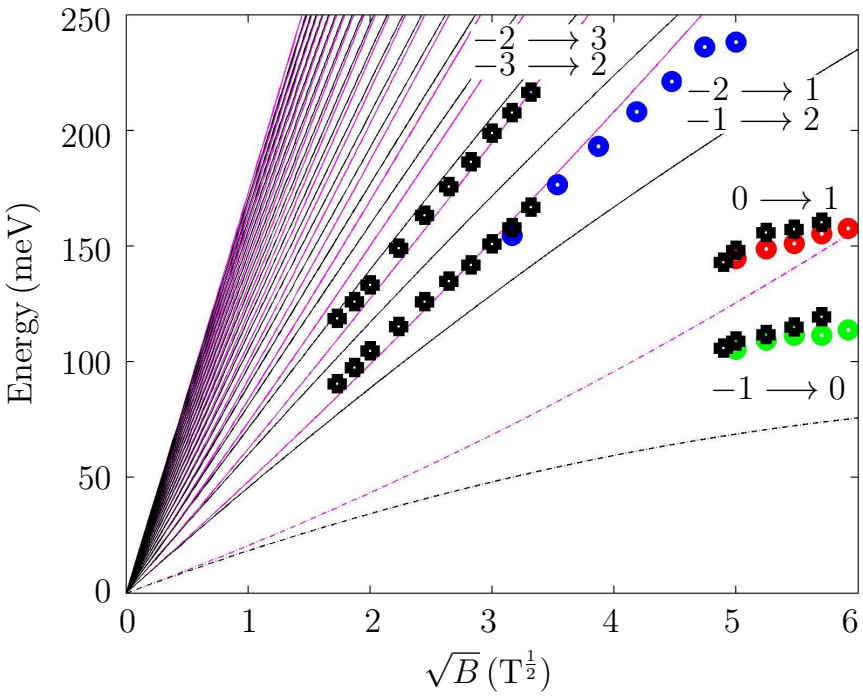

Fig. 6.2: Experimentally determined position of inter-Landau level resonances in BiTeI. The individual points were obtained from spectra in Fig. 5.7. A part of the data (black crosses) are taken from another high-field experiment, provided by Dr. Bordács.

Note the assignment of these transitions which refers to Fig. 6.1 and is consistent with Ref. [7]. Further measurements with a defined circular polarization are needed to definitely confirm this tentative yet probable assignment. The two pronounced transitions at low energies (113.7 and 157.6 meV at 35 T) have been identified as 0⟶1 and -1⟶0 transitions. These are expected to be degenerate in an ideal system of massless Dirac-type particles; nevertheless, they should split in their energies when a real electronic band structure of BiTeI, with a pronounced electron-hole asymmetry, is considered. The theoretical model predicts many inter-Landau level transitions with roughly the same intensities, yet we have observed only three of them. Additional measurements with a circularly resolved polarization would provide information on whether or not the transition is active in one or other polarization. Unfortunately, it is not possible to perform such a measurements at this moment. The probe for the high-field measurements is not designed for this purpose. On the other hand, such a measurement would probably reveal the fact that the transitions are active in both polarizations, thus degenerated. As discussed later on, the lack of splitting between, for instance -1⟶2 and -2⟶1 transitions indicates limits of validity of a simple Rashba-type Hamiltonian for the conduction band of BiTeI. Counterintuitively, the real system exhibits lower electron-hole asymmetry as compared to predictions of this model.

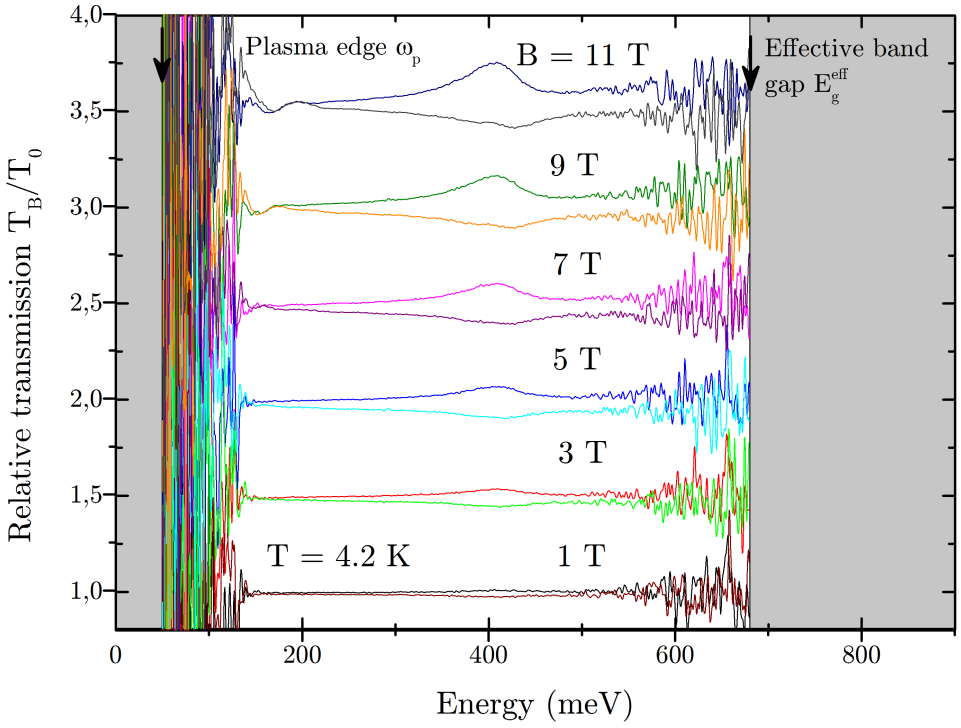

Fig. 6.3: The relative transmission spectra in both σ^+ and σ^- polarizations for BiTeI.

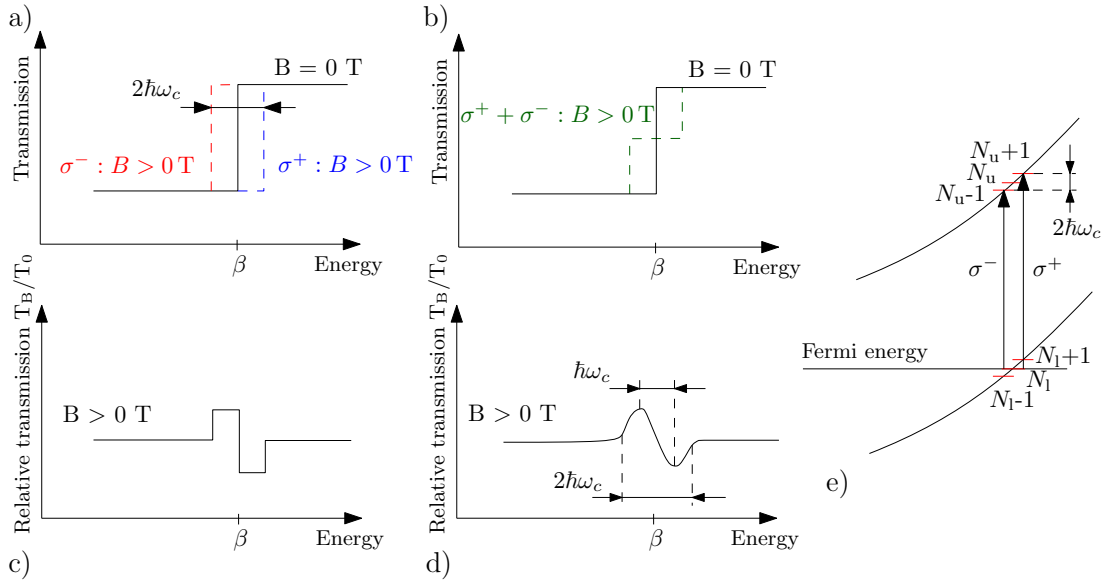

Fig. 6.4: Schematic sketch of the wavy feature origin, where a) a splitting of the transmission onset with respect to both polarizations equals to $2\hbar\omega_c$, b) the shape of the transmission onset in the magnetic field, c) the relative transmission for an ideal case, d) is a real skewed shape of the relative transmission around the β energy and e) shows the energy difference between polarizations around the β energy in the band structure.

The high-energy (in Fig. 6.1 d) yellow-highlighted) region is characterized by a wavy spectral feature positioned at energy of β transition in the zero-field transmission spectrum. Its position varies in different BiTeX materials and also slightly depends on the particular density of charge carriers in the conduction band. The origin of this feature can be trivially explained as a splitting of the transmission onset with respect to both σ^+ and σ^- polarizations[1, 2] in the magnetic field, see Fig. 6.1 c). The magnitude of this splitting equals to $2\hbar\omega_c$ as shown in Fig. 6.4 a),e). Considering the shape of the transmission in the magnetic field as a sum of both polarizations, see Fig. 6.4 b), we can directly obtain the shape of this feature from a simple division by a transmission at zero field. Figure 6.4 c) shows the shape of the wavy feature for an ideal case, though the real shape is slightly skewed and blurred as shown in Fig. 6.4 d). To confirm our conclusion, additional measurements have been performed at low magnetic fields. We added a polarizer and a zero-order quarter-wave plate twisted by an angle of $\pi/4$ to circularly polarize the light. The observed dependence of the magneto-transmission on the helicity of the probing radiation is in perfect agreement with our simple model. The result can be seen in Fig. 6.3 which is a clear evidence of the veracity of our claim. The relative transmission spectra measured for BiTeI material are clearly polarization-resolved. This measurement also verifies the theory of transition degeneracy. Both polarization resolved relative transmission spectra at 11 T show a dip around 165 meV, thus confirming our hypothesis. Moreover, splitting between polarizations increases with the magnetic field following the $2\hbar\omega_c$ dependence.

On top of that, an effective mass can be derived out of a cyclotron resonance. The energy difference 25.5 meV between maximum and minimum for 11 T was determined from the graph and approximated as $\hbar\omega_c$, see Fig. 6.4 d). The calculated value of the effective mass is $m^* = 0.05m_0$, m_0 being the mass of a free electron. This value is almost half of the value derived from the first principle calculations [7]; nevertheless, our approximation may not be accurate. This essentially simple experiment supports our previous intuitive statements and thus confirms the origin of the wavy feature around the β energy. According to the simple Rashba model, the position of the β energy is strongly dependent on doping, i.e., as a function of the carrier density. However, we do not see such a dependence in our experimental data; either that, or it is very weak. The same conclusion can be found in a work of Demkó [36]. This is another indication of a limited validity of the Rasha model for BiTeX compounds. In the following sections, we present the output of the theoreti-

[1] σ^+ is a polarization of light which induces inter-Landau level transitions between LLs with a increasing index, e.g., -1 $\longrightarrow$ 2, -3 $\longrightarrow$ 4, etc.

[2] On the other hand σ^- is a polarization of light which induces inter-Landau level transitions between LLs with a decreasing index, e.g., -2 $\longrightarrow$ 1, -4 $\longrightarrow$ 3, etc.

cal model as a simulation of the relative transmission spectra shape which will be compared with the real data.

6.2 Simulations

In order to obtain the theoretically expected response of BiTeI in the magneto-transmission experiment, we need to calculate the transmission through the plan-parallel slab. This transmission can be expressed in a simplified form such as a sum of the geometric series $a/(1-q)$:

$$T^{\pm}_{B,0} = \frac{(1-r_{\pm})^2 \exp\left[(-2\omega\kappa_{\pm}d)/c\right]}{1-r_{\pm}^2 \exp\left[(-4\omega\kappa_{\pm}d)/c\right]}, \tag{6.1}$$

where $r_{\pm}$ is the reflection coefficient, $\kappa_{\pm}$ is an imaginary part of the refractive index and d is the thickness of the plan-parallel slab which is in our case $d = 2\,\mu\text{m}$. Both the field and zero-field transmissions in a linearly polarized light are an average of both circular polarization transmissions:

$$T_{B,0} = \left(T^{+}_{B,0} + T^{-}_{B,0}\right)/2. \tag{6.2}$$

The final output of the calculations is the relative transmission which is a ratio of T_B and T_0. To avoid problems with calculations of the zero-field response, which require a more elaborated approach than the below presented Kubo-Greenwood formula, Eq. (6.6), we replace the zero-field spectra by that calculated at $B = 1$[3]. This approximation gives reasonable results, the provided separation of adjacent inter-LL resonances is smaller than the phenomenologically introduced broadening.

However, to be able to calculate the transmission spectrum through such a slab, we have to know the reflection coefficient which is given as:

$$|r_{\pm}| = \sqrt{\frac{(1-n_{\pm})^2 + \kappa_{\pm}^2}{(1+n_{\pm})^2 + \kappa_{\pm}^2}}, \tag{6.3}$$

therefore, the complex refractive index has to be known. Although we do not know the complex refractive index yet, it can be expressed in terms of real and imaginary parts using the response function. The most elegant way is to calculate the real and imaginary part of the refractive index using the polarization-resolved optical conductivity as:

$$n_{\pm}(\omega, B) = \sqrt{\frac{1}{2}\left\{\sqrt{\left(\frac{1-\sigma_{2\pm}}{\omega\varepsilon_0}\right)^2 + \left(\frac{\sigma_{1\pm}}{\omega\varepsilon_0}\right)^2} + \frac{1-\sigma_{2\pm}}{\omega\varepsilon_0}\right\}}, \tag{6.4}$$

[3]There is no visible difference between transmission at 0 T and 1 T.

$$\kappa_{\pm}(\omega, B) = \sqrt{\frac{1}{2}\left\{\sqrt{\left(\frac{1-\sigma_{2\pm}}{\omega\varepsilon_0}\right)^2 + \left(\frac{\sigma_{1\pm}}{\omega\varepsilon_0}\right)^2} - \frac{1-\sigma_{2\pm}}{\omega\varepsilon_0}\right\}}. \tag{6.5}$$

The computation of the optical conductivity is a challenging theoretical task, the complexity of which depends on the chosen level of the approximations. In our simplified approach, we limited ourselves to a simple linear-response Kubo-Greenwood formula [52, 53] and introduced a purely phenomenological line broadening Γ. We write:

$$\begin{aligned}\sigma_{\pm}(\omega, B) = \text{valley deg.} \cdot \text{spin deg.} \cdot \text{LL deg.} \cdot \frac{e^2}{\omega d} \cdot \\ \cdot \sum_{k_z, M, N} \mathrm{i} \frac{|x_{\pm}|^2}{E_M - E_N - \hbar\omega + \mathrm{i}\Gamma} \left[f_N(k_z) - f_M(k_z)\right],\end{aligned} \tag{6.6}$$

where $E_M - E_N$ are the transition energies between M, N levels. To get the transition energies, we have to first calculate the LLs energies by using the modified Eq. (2.14) where the simple Rashba Hamiltonian is extended by the term containing a g-factor, resulting in the Landau level spectrum as follows:

$$E_{\pm N} = \hbar\omega_c N \pm \sqrt{\left(\frac{\hbar\omega_c}{2} + \frac{g\mu_B B}{2}\right)^2 + 2v_{\mathrm{F}}^2 e\hbar B N} + \frac{\hbar^2 k_z^2}{2m_0} \qquad N = 0, 1, 2, ..., \tag{6.7}$$

where the $\mu_B = e\hbar/(2m_0) = 9.27400915 \times 10^{-24}\,\mathrm{J}\cdot\mathrm{T}^{-1}$ is a Bohr magneton and the entire extension term is responsible for a shift in energy of all the LLs. We calculated the transition energies by simply deducing all the LLs energies from each other, following the optical excitations selection rule known for Dirac systems as $\pm N \longrightarrow \pm|N \pm 1|$. There is a series of inter-Landau level transitions satisfying these selection rules, therefore we must distinguish between them. For instance, the -1$\longrightarrow$2 transition is called the interband transition, whereas the -2$\longrightarrow$-1 or 1$\longrightarrow$2 are called the intraband transitions. We have chosen this type of notation to simplify the orientation, even though everything happens within the conduction band. A valley deg. as well as a spin deg. equals 1 and LL deg. equals eB/h. f_N and f_M are the occupancies of the relevant LLs. If we sum over all M, N for $E_M > E_N$ and $f_N(k_z) - f_M(k_z) > 0$ we get[4]:

[4]This condition is fulfilled for $M = 0, \pm1, \pm2, ...$ and $N = M - 1$.

$$\sigma_{\pm}(\omega, B) = \frac{e^3 B}{h\omega} \frac{1}{d} 2 \frac{d}{2\pi} \int \mathrm{d}k_z \sum_{M,N} \mathrm{i} \frac{|x_{\pm}|^2}{E_M - E_N - \hbar\omega + \mathrm{i}\Gamma} =$$
$$= \frac{e^3 B}{h\omega\pi} \Delta k_z \sum_{M,N} \mathrm{i} \frac{|x_{\pm}|^2}{E_M - E_N - \hbar\omega + \mathrm{i}\Gamma} \ , \tag{6.8}$$

where Δk_z scales the Lorentzian function with respect to a transition intensity. Noteworthy is the behavior of the LLs below the crossing point. In a certain magnetic field they flip over and their energies start to increase. This effect can be observed even at low fields for a high index[5] N. Since our system is 3D, the dispersion of the LLs in the z direction should also be considered. The dispersion of the LLs along the z direction is purely parabolic and has interesting consequences. Only transitions from the occupied to the free levels are allowed for the semiconductors. This also applies for BiTeX materials; however, due to the third dimension we might observe transitions between the LLs which are below the Fermi level, thus both occupied. At some point, the parabolic dispersion makes the LLs below the Fermi level cross it, thus allowing transitions between those LLs, see Fig. 3.4. Altogether, there are three configurations:

$$\Delta k_z = \begin{cases} 0 & \text{for } E_M \ \& \ E_N > E_\mathrm{F}, \\ \sqrt{E_\mathrm{F} - E_N}\sqrt{2m_0}/\hbar & \text{for } E_M > E_\mathrm{F} \ \& \ E_N < E_\mathrm{F}, \\ \sqrt{E_\mathrm{F} - E_N}\sqrt{2m_0}/\hbar - \sqrt{E_\mathrm{F} - E_M}\sqrt{2m_0}/\hbar & \text{for } E_M \ \& \ E_N < E_\mathrm{F}, \end{cases} \tag{6.9}$$

where $M = 0, \pm1, \pm2, ...$ and $N = M - 1$. Since the mass m^* in our system is anisotropic, we consider in-plane mass m^* for k_x and k_y direction and out-of-plane mass $m^* = m_0$ for k_z direction. $|x_{\pm}|^2 = |\langle M_{\pm}|\widehat{v}_{\pm}|N_{\pm}\rangle|^2$ are the velocity matrix elements, $|M_{\pm}\rangle$ and $|N_{\pm}\rangle$ being the M-th and N-th state, where $M = N \pm 1$ depending on the polarization, as:

$$|N_{\pm}\rangle = \begin{bmatrix} \alpha_N^{\pm}|N\rangle \\ \beta_N^{\pm}|N-1\rangle \end{bmatrix} \ , \tag{6.10}$$

where $\alpha_N^{\pm}$ and $\beta_N^{\pm}$ are the complex coefficients and their form is left to the Appendix B. The velocity operators $\widehat{v}_{\pm}$ are given as:

$$\widehat{v}_{+} = \begin{pmatrix} \frac{\hbar}{m^*}\frac{a^\dagger}{l_B} & 0 \\ -\sqrt{2}\mathrm{i}\frac{\alpha_\mathrm{R}}{\hbar} & \frac{\hbar}{m^*}\frac{a^\dagger}{l_B} \end{pmatrix} \quad \widehat{v}_{-} = \begin{pmatrix} \frac{\hbar}{m^*}\frac{a}{l_B} & \sqrt{2}\mathrm{i}\frac{\alpha_\mathrm{R}}{\hbar} \\ 0 & \frac{\hbar}{m^*}\frac{a}{l_B} \end{pmatrix} \ , \tag{6.11}$$

[5]Interesting fact: To have only one Landau level below the crossing point in our system, a magnetic field of more than 400 T would be needed.

where $l_B = \sqrt{\hbar/(eB)}$ is a magnetic length. The velocity matrix operators account for the selection rules governing the optically active transitions and details of their calculation are left also to the Appendix B. Another important thing, which has not been considered yet, are the negative frequencies and the tails of the Lorentzian functions in low energies. Formally, optical conductivity for negative frequencies corresponds to the opposite circular polarization of radiation. The finite phenomenological broadening of the Lorentzian functions implies that the tails contribute to the polarization in which non-broadened resonances are not active. In order to illustrate the plausibility of our calculations we compare the shape of the calculated relative reflectivity with the experimental data measured by Dr. Bordács in Grenoble. A comparison of the simulated relative reflectivity and the experimental data is shown in Fig. 6.5.

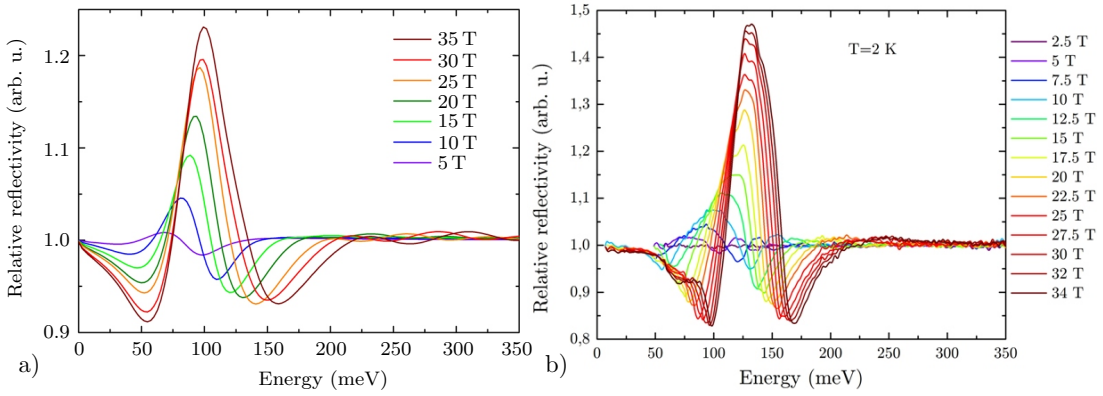

Fig. 6.5: Comparison of a) the simulated relative reflectivity at fields of up to 35 T and b) the experimental data measured on the BiTeI sample - printed with kind permission from Dr. Bordács.

Location of the relative reflectivity maxima is most probably related to the position of the plasma edge which is different for samples with a different carrier density. However, the shape of the spectra is in good agreement. Another sign of the calculations' plausibility is the polarization-resolved β energy splitting as described in Fig. 6.4. Figure 6.6 a) shows an absolute transmission spectra at zero field (black curve) and the transmission spectra for both polarizations in the magnetic field. The transmission curve behaves as it should and the transmission goes to zero below the plasma edge. Moreover the polarization-resolved β energy splitting creates the wavy feature in the relative transmission spectra right at the same energy, see Fig. 6.6 b). As we concluded, the scripts are programmed correctly and we may proceed with quantitative comparison of our calculations with the experimental data presented in the next Chapter.

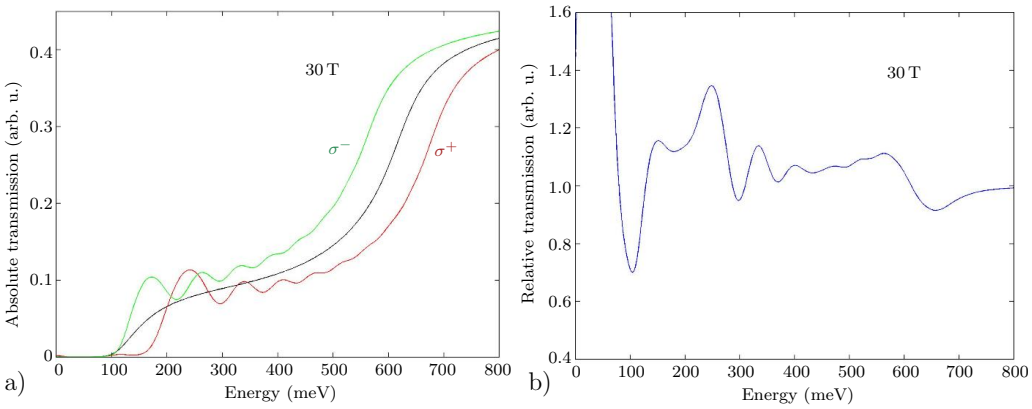

Fig. 6.6: The simulation of a) the absolute transmission at zero field with a clear polarization-resolved β energy splitting in a magnetic field and b) the relative transmission with a wavy feature right at the β energy.

7 COMPARISON OF THE EXPERIMENTAL DATA WITH THE SIMULATIONS

In this Chapter we present results of our theoretical calculations optimized to reproduce the observed response of BiTeX materials in the magneto-transmission experiment. The optimization process lies in the finding of an individual parameters which are included in our theoretical model described in detail in the previous Chapter. These are: the effective g-factor, the Fermi energy (taken as independent of the magnetic field), the effective electron mass m*, the Fermi velocity (the strength of the Rashba coupling parameter) and the line broadening parameter. We define the position of the Dirac point as zero-energy and to facilitate the optimization procedure, we have decided to keep the line broadening and the effective mass constant, using values, $\Gamma = 40\,\mathrm{meV}$ and $m^* = 0.09m_0$, reported in Ref. [7]. The Fermi velocity $v_\mathrm{F} = 0.535 \times 10^6\,\mathrm{m/s}$ is calculated from the slope of the transition energies marked with blue circles in Fig. 6.2, corresponding to the blue arrows in Fig. 7.1. The two remaining parameters, the Fermi energy and the effective g-factor may be deduced when we consider the field-evolution of the response due to the inter-Landau level transitions involving $N = 0$ LL. The $0 \longrightarrow 1$ transition marked with the red arrows increases in its intensity, implying the negative slope of the $N = 0$ LL. The simultaneous observation of both $-1 \longrightarrow 0$ and $0 \longrightarrow 1$ transitions,

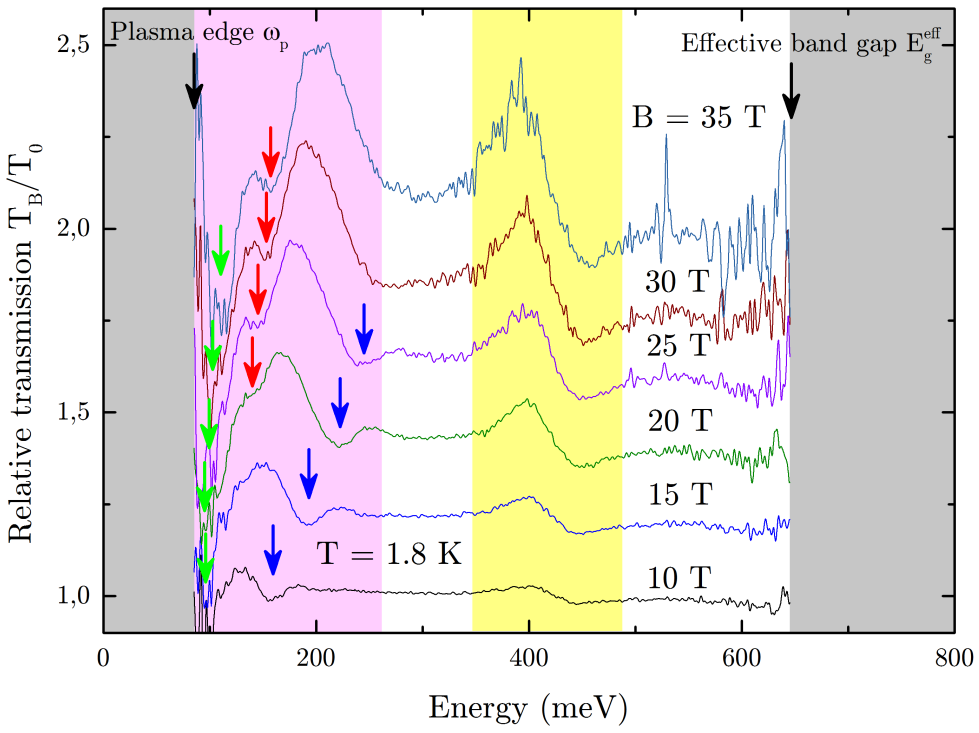

Fig. 7.1: The experimental relative transmission spectra measured up to 35 T.

with roughly the same apparent intensities, see Fig. 7.1, implies the Fermi level lying slightly above the Dirac point. Furthermore, even at high fields the Fermi level has to be above the $N = 0$ LL; otherwise, it would lead to a disappearance of the $0 \longrightarrow 1$ transition which is undesirable. Moreover, we do still see this transition in the experimental data in high fields. The separation between $-1 \longrightarrow 0$ and $0 \longrightarrow 1$ resonances allows us to estimate the effective g-factor which is within the Rashba model, together with the effective mass, responsible for the linear with B dispersion of the $N = 0$ LL. Namely, at $B = 35\,\mathrm{T}$ this splitting reaches $\sim 50\,\mathrm{meV}$. It contains two contributions: the cone asymmetry and the Zeeman effect due to the g-factor. The upper value of the cone asymmetry may be estimated when we consider the evolution of $-2 \longrightarrow 1$ and $-1 \longrightarrow 2$ transitions. Since no clear splitting is observed, the cone asymmetry cannot exceed 15% which would translate into the splitting of $-1 \longrightarrow 0$ and $0 \longrightarrow 1$ resonances by roughly 20 meV. The rest is due to the Zeeman effect. To explain the experimentally observed splitting of $\sim 50\,\mathrm{meV}$, we have to consider a relatively large value of the effective g-factor, $g = -17 \pm 2$ as estimated from the g-factor term $\Delta E = g\mu_B B/2$. Since the splitting of 30 meV corresponds to a double change of the transition energies as the energy of one increases and the other decreases by the same amount when the $N = 0$ LL tilted, we get the energy

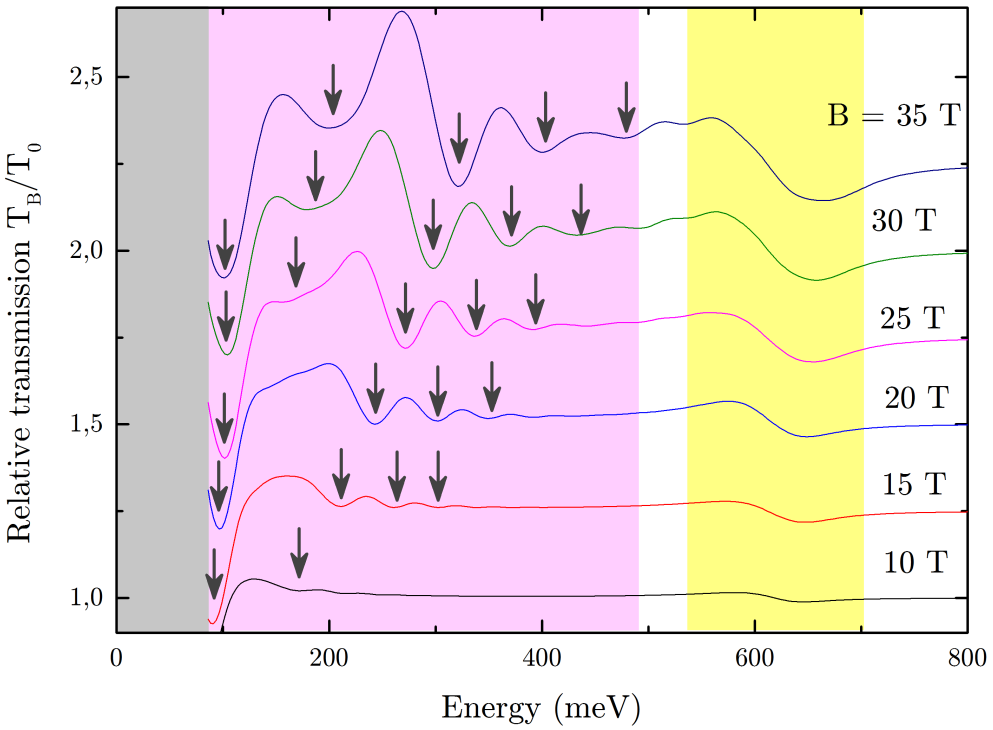

Fig. 7.2: The simulated relative transmission spectra up to 35 T with following parameters: $g = -17$ and $E_F = 20\,\mathrm{meV}$. The spectral features having nearly $\sqrt{B}$ field-dependence are denoted by vertical black arrows.

difference $\Delta E = 15\,\mathrm{meV}$.

Using parameters deduced and taken from literature we may calculate the theoretically expected magneto-transmission spectra and compare to the experimental data. The energy of the Fermi level is optimized in order to achieve as similar shape of the spectra as possible. The optimal Fermi energy seems to be 20 meV which is close to the one determined in Ref. [7]. Figure 7.2 shows the magneto-transmission spectra where we can see, similarly as in the experimental data, an induced transmission around 200 meV. The grey arrows indicate stark spectral features evolving with magnetic field as $\sqrt{B}$ in the pink-highlighted region. However, mostly in the low frequencies it does not reproduce the positions of the resonances as also evidenced in Fig. 6.2. Furthermore, in the Rashba model the energy of $N = 0$ LL significantly increases with respect to the cyclotron frequency. To suppress this contribution we use the negative effective g-factor. As shown in Fig. 7.3 b), for $g = -17$ has the $N = 0$ LL still increasing tendency and even lower g-factor would be needed to obtain the negative slope of this level allowing to explain the increasing intensity of the $0 \longrightarrow 1$ transition. Yet the g-factor would be unrealistically low.

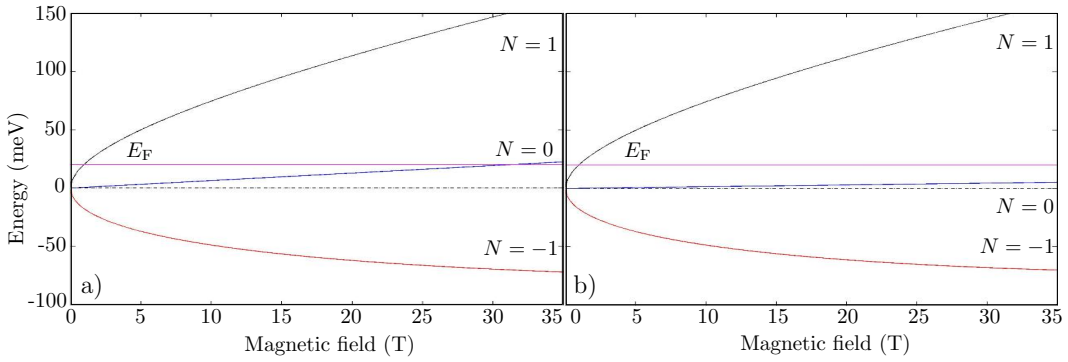

Fig. 7.3: The dependence of the zero-Landau level on the magnetic field with a) $g = 0$ and b) $g = -17$. The purple line indicates the position of the Fermi energy, here $E_F = 20\,\mathrm{meV}$.

One of the fundamental differences between the experimental data and the simulations is the position of the wavy feature in yellow highlighted region. It is shifted towards higher energies for simulated spectra. The most logical explanation for this is the simplicity of the Rashba model which implies fully parabolic bands in the limit of high momenta. In fact, the electronic band structure becomes linear with increasing distance from the Dirac point. This is confirmed also by the numerical ab-initio calculations of the electronic band structure, see e.g., [6,18]. The cone is possibly better defined with a lower asymmetry. On the other hand, the experimental data may serve to derive an effective mass in the outer Fermi surface where a simple formula

$E_\beta = m^*_{\text{out}} \cdot v_{\text{F}}^2$ holds. For β energy $\sim$400 meV (determined from the experimental data) and the Fermi velocity $v_{\text{F}} = 0.535 \times 10^6$ m/s we get $m^*_{\text{out}} = 0.25 m_0$, which is slightly higher, however in good agreement with the paper of Murakawa [49]. The second essential difference is absence of the well-resolved inter-Landau level transitions with higher indices in the experimental data. As previously mentioned, these transitions are very likely degenerate in energy with respect to the polarization and subsequently are no longer resolved in spectra above 25 T. Whereas Rashba model implies rather big splitting of twice the cyclotron frequency, hence 2.6 meV/T. This value produces a splitting of $\sim$80 meV for the magnetic field 30 T which is well visible in the theoretically calculated spectra in Fig. 7.2 where splitting at 30 T equals 76 meV. The evolution of the discussed inter-Landau level transitions is illustrated in Fig. 7.4. It is possible to qualitatively reproduce the shape of the relative transmission spectra very well; however, with significant quantitative deviations. Therefore, we conclude that the simple Rashba model provides us with a very good qualitative description of the observed magneto-optical response of BiTeI; however, it fails to describe the experimental data quantitatively.

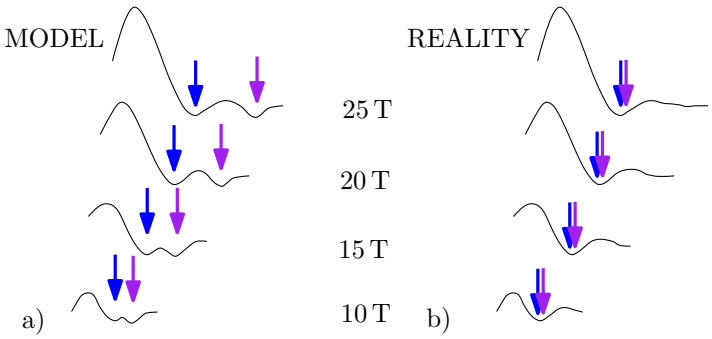

Fig. 7.4: The evolution of the higher index inter-Landau level transitions with respect to the magnetic field. Where a) shows the splitting of twice the cyclotron frequency whereas b) the degeneracy of the transitions.

8 CONCLUSIONS

The BiTeX materials (X=I, Br, Cl) are known for many years; however, only recently interesting properties have been discovered. Ever since, many experiments have been performed in order to explore and describe the attributes of these materials and their electronic band structure; nevertheless, it is the recent discovery of giant Rashba-type spin splitting which renewed the interest into these compounds. In this thesis, we used the infrared magneto-spectroscopy to experimentally probe effects related to the RSS. Interestingly, the RSS gives rise to an appearance of the massless Dirac fermions in the vicinity of the crossing point (Dirac point). This novel kind of Dirac particles extends the current family of Dirac-type materials such as graphene, topological insulators or 3D Dirac and Weyl semimetals.

We have performed an extensive magneto-transmission study for different materials in a wide range of photon energies and magnetic fields. This allowed us to observe the evolution of the spin-polarized $N = 0$ Landau level in BiTeI. A further analysis lead to estimates for the effective g-factor which turned out to be a considerable contribution to this work. Mainly because this information cannot be derived from the magneto-transport measurements, neither from standard electron spin resonance (ESR) experiments. To facilitate the interpretation of the experimental data, we have chosen the simple Rashba model which is nowadays widely used to describe BiTeX materials. The theoretically expected magneto-transmission and magneto-reflectivity spectra were calculated, compared to the experimental data and critically evaluated.

Surprisingly, the Dirac cone in the center of BiTeI Brillouin zone is much better defined as compared to the simple Rashba model predictions, i.e. has significantly lower electron-hole asymmetry which is also evidenced by the ab-initio band structure calculations. In conclusion, the simple Rashba model rather well describes the electronic band structure of BiTeX materials at the qualitative level; therefore, it may be successfully used for the analysis of their magneto-optical response. BiTeX materials thus represent another class of solid-state systems to which this fairly old model becomes applicable. On the other hand, the simplicity of the Rashba model, which implies only two tunable parameters, does not allow quantitative description of our experimental data.

APPENDICES

Appendix A - Landau level spectrum

In this appendix, we will calculate the Landau level spectrum of a system with a simple Rashba-type coupling between orbital motion of electrons and their spin degree of freedom. The corresponding Hamiltonian reads:

$$H = \frac{p^2}{2m^*} + \frac{\alpha_{\mathrm{R}}}{\hbar}(\vec{e}_z \times \vec{p}) \cdot \vec{\sigma}, \tag{A.1}$$

where $\vec{e}_z = (0, 0, 1)$ is the unit vector in the z-direction and $\vec{\sigma}$ are the Pauli matrices:

$$\sigma_x = \begin{pmatrix} 0 & 1 \\ 1 & 0 \end{pmatrix} \quad \sigma_y = \begin{pmatrix} 0 & -\mathrm{i} \\ \mathrm{i} & 0 \end{pmatrix} \quad \sigma_z = \begin{pmatrix} 1 & 0 \\ 0 & -1 \end{pmatrix} . \tag{A.2}$$

The cross product of the unit vector $\vec{e}_z$ and the momentum operator $\vec{p}$ implies that the free electron dispersion (the first term in Eq. (A.1)) is modified only in the xy plane.

$$(\vec{e}_z \times \vec{p}) = \begin{bmatrix} \vec{\imath} & \vec{\jmath} & \vec{k} \\ 0 & 0 & 1 \\ p_x & p_y & 0 \end{bmatrix} = (-p_y, p_x, 0). \tag{A.3}$$

The multiplication of the cross product by the Pauli matrices and simple mathematical treatment lead to the Hamiltonian which is well-known from literature, see e.g. Ref. [54]:

$$H = \begin{pmatrix} p^2/(2m^*) & -\mathrm{i}\frac{\alpha_{\mathrm{R}}}{\hbar}p^- \\ \mathrm{i}\frac{\alpha_{\mathrm{R}}}{\hbar}p^+ & p^2/(2m^*), \end{pmatrix} \tag{A.4}$$

where $p^+ = p_x + \mathrm{i}p_y$ and $p^- = p_x - \mathrm{i}p_y$. When we define the creation and annihilation operators in the standard way, $p^+ = a\sqrt{2e\hbar B}$ and $p^- = a^\dagger\sqrt{2e\hbar B}$, respectively, we obtain:

$$\begin{aligned} p_x^2 + p_y^2 &= \frac{1}{2}(p^+p^- + p^-p^+) = \frac{1}{2}(2e\hbar B a a^\dagger + 2e\hbar B a^\dagger a) = \\ &= 2e\hbar B\frac{1}{2}(aa^\dagger + a^\dagger a) = 2e\hbar B\frac{1}{2}(a^\dagger a + 1 + a^\dagger a) = \\ &= 2e\hbar B(a^\dagger a + \frac{1}{2}) \ , \end{aligned} \tag{A.5}$$

where anticommutation relation $\left[a, a^\dagger\right] = aa^\dagger - a^\dagger a = 1$ was used, therefore $aa^\dagger = a^\dagger a + 1$. This momentum containing magnetic field can be substituted into the matrix in Eq. (A.4), where $p^2 = p_x^2 + p_y^2 + p_z^2$. Note that the motion in the z-direction is not

affected by the Rashba coupling and the corresponding dispersion remains parabolic. Using the derived Hamiltonian, we solve Schrödinger's equation $H|\varphi\rangle = E_N|\varphi\rangle$, searching for a solution using the ansatz for the wave function $\begin{pmatrix} \alpha|N\rangle \\ \beta|N-1\rangle \end{pmatrix}$:

$$\begin{pmatrix} \frac{\hbar^2 k_z^2}{2m^*} + \frac{e\hbar B}{m^*}(a^\dagger a + \frac{1}{2}) & -\mathrm{i}\frac{\alpha_\mathrm{R}}{\hbar}\sqrt{2e\hbar B}a^\dagger \\ \mathrm{i}\frac{\alpha_\mathrm{R}}{\hbar}\sqrt{2e\hbar B}a & \frac{\hbar^2 k_z^2}{2m^*} + \frac{e\hbar B}{m^*}(a^\dagger a + \frac{1}{2}) \end{pmatrix} \begin{pmatrix} \alpha|N\rangle \\ \beta|N-1\rangle \end{pmatrix} = \\ = \begin{pmatrix} \frac{\hbar^2 k_z^2}{2m^*} + \frac{e\hbar B}{m^*}(N + \frac{1}{2}) & -\mathrm{i}\frac{\alpha_\mathrm{R}}{\hbar}\sqrt{2e\hbar B}\sqrt{N} \\ \mathrm{i}\frac{\alpha_\mathrm{R}}{\hbar}\sqrt{2e\hbar B}\sqrt{N} & \frac{\hbar^2 k_z^2}{2m^*} + \frac{e\hbar B}{m^*}(N - \frac{1}{2}) \end{pmatrix} \begin{pmatrix} \alpha \\ \beta \end{pmatrix} = E_N \begin{pmatrix} \alpha \\ \beta \end{pmatrix}. \tag{A.6}$$

This eigenvalue problem has a non-trivial solution if and only if the determinant $\det(H - E_N I)$ equals zero where I is an unit matrix. In our system the determinant has a form as:

$$\det \begin{pmatrix} \frac{\hbar^2 k_z^2}{2m^*} + \frac{e\hbar B}{m^*}(N + \frac{1}{2}) - E_N & -\mathrm{i}\frac{\alpha_\mathrm{R}}{\hbar}\sqrt{2e\hbar B}\sqrt{N} \\ \mathrm{i}\frac{\alpha_\mathrm{R}}{\hbar}\sqrt{2e\hbar B}\sqrt{N} & \frac{\hbar^2 k_z^2}{2m^*} + \frac{e\hbar B}{m^*}(N - \frac{1}{2}) - E_N \end{pmatrix} = 0, \tag{A.7}$$

where we label some expressions as $A = \hbar^2 k_z^2/(2m^*)$, $B = e\hbar B/m^*$ and $C = 2e\hbar BN\alpha_\mathrm{R}^2/(\hbar^2)$ in order to simplify the notation. Finally, the solved problem reduces down to a simple quadratic equation:

$$E_N^2 - (2A + 2BN)E_N + A^2 + 2ABN + B^2N^2 - \left(\frac{B}{2}\right)^2 - C = 0, \tag{A.8}$$

with the solution:

$$E_N = BN \pm \sqrt{\left(\frac{B}{2}\right)^2 + C} + A. \tag{A.9}$$

By substituting the expressions again instead of using the letters A, B, C, we obtain a set of eigenvalues, so-called Landau level spectrum:

$$E_{\pm N} = \hbar\omega_c N \pm \sqrt{\left(\frac{\hbar\omega_c}{2}\right)^2 + 2v_\mathrm{F}^2 e\hbar BN} + \frac{\hbar^2 k_z^2}{2m^*}, \tag{A.10}$$

where $\omega_c = eB/m^*$ and $v_\mathrm{F}^2 = \alpha_\mathrm{R}^2/\hbar^2$.

Appendix B - Velocity matrix elements

This appendix is devoted to a calculation of the velocity matrix elements needed within the Kubo-Greenwood formalism. To perform this calculation, complex coefficients $\alpha_N^{\pm}$ and $\beta_N^{\pm}$ are required. These complex coefficients were calculated in Ref. [9] and have the following form:

$$\alpha_N^{\pm} = \frac{c}{\sqrt{2(b^2+c^2 \mp b\sqrt{b^2+c^2})}} \; ; \quad \beta_N^{\pm} = \mathrm{i}\frac{b \mp \sqrt{b^2+c^2}}{\sqrt{2(b^2+c^2 \mp b\sqrt{b^2+c^2})}} \; , \tag{B.1}$$

where $b = \hbar\omega_c/2 + g\mu_B B/2$ and $c = \sqrt{2}\sqrt{N}\alpha_{\mathrm{R}}/l_B$. For $N = 0$ the coefficients have special form where $\alpha_0^{\pm} = 1$ and $\beta_0^{\pm} = 0$, therefore Eq. (6.10) yields:

$$|0\rangle = \begin{bmatrix} |0\rangle \\ 0 \end{bmatrix} \tag{B.2}$$

Let us now calculate the velocity matrix elements for the interband transitions where "interband" refers to transitions from levels originating in the lower dispersion branch ("$-$" in $N_{\pm}$) to levels belonging to the upper branch ("$+$" in $N_{\pm}$). For the σ^+ polarization, which is connected to $\widehat{v}_+$, we start using equation $\langle M_+|\widehat{v}_+|N_-\rangle$ where $M_+ = N_+ + 1$:

$$\begin{aligned}
&\langle N_+ + 1|\widehat{v}_+|N_-\rangle = \\
&= \left[\left(\alpha_{N+1}^+\right)^* \langle N+1| \; ; \; \left(\beta_{N+1}^+\right)^* \langle N| \; \right] \begin{bmatrix} \frac{\hbar}{m^*}\frac{a^\dagger}{l_B} & 0 \\ -\sqrt{2}\mathrm{i}\frac{\alpha_{\mathrm{R}}}{\hbar} & \frac{\hbar}{m^*}\frac{a^\dagger}{l_B} \end{bmatrix} \begin{bmatrix} \alpha_N^-|N\rangle \\ \beta_N^-|N-1\rangle \end{bmatrix} = \\
&= \left[\left(\alpha_{N+1}^+\right)^* \langle N+1| \; ; \; \left(\beta_{N+1}^+\right)^* \langle N| \; \right] \begin{bmatrix} \frac{\hbar}{m^*}\frac{\sqrt{N+1}}{l_B}\alpha_N^-|N+1\rangle \\ -\sqrt{2}\mathrm{i}\frac{\alpha_{\mathrm{R}}}{\hbar}\alpha_N^-|N\rangle + \frac{\hbar}{m^*}\frac{\sqrt{N}}{l_B}\beta_N^-|N\rangle \end{bmatrix} = \\
&= \frac{\hbar}{m^*}\frac{\sqrt{N+1}}{l_B}\left(\alpha_{N+1}^+\right)^*\alpha_N^- + \left(\beta_{N+1}^+\right)^*\left[\frac{\hbar}{m^*}\frac{\sqrt{N}}{l_B}\beta_N^- - \sqrt{2}\mathrm{i}\frac{\alpha_{\mathrm{R}}}{\hbar}\alpha_N^-\right] \; ,
\end{aligned} \tag{B.3}$$

where the squared absolute value of this expression enters into the Kubo-Greenwood formula. Analogously, we have calculated the matrix elements for other inter-Landau level transitions, for both interband and intraband transitions in both circular polarizations. Therefore, we will submit only the results itself. The velocity matrix elements for the interband inter-Landau level transitions and σ^- polarization, which is connected to $\widehat{v}_-$, are given as:

$$\begin{aligned}
&\langle N_+|\widehat{v}_-|N_- + 1\rangle = \\
&= \left(\alpha_N^+\right)^*\left[\frac{\hbar}{m^*}\frac{\sqrt{N+1}}{l_B}\alpha_{N+1}^- + \sqrt{2}\mathrm{i}\frac{\alpha_{\mathrm{R}}}{\hbar}\beta_{N+1}^-\right] + \alpha_N^- + \frac{\hbar}{m^*}\frac{\sqrt{N}}{l_B}\left(\beta_N^+\right)^*\beta_{N+1}^- \; .
\end{aligned} \tag{B.4}$$

That would be all for interband inter-Landau level transitions (between both branches). The velocity matrix elements for the intraband inter-Landau level transitions within upper branch and σ^+ polarization are given as:

$$\begin{aligned}&\langle N_+ + 1|\widehat{v}_+|N_+\rangle = \\ &= \frac{\hbar}{m^*}\frac{\sqrt{N+1}}{l_B}\left(\alpha^+_{N+1}\right)^*\alpha^+_N + \left(\beta^+_{N+1}\right)^*\left[\frac{\hbar}{m^*}\frac{\sqrt{N}}{l_B}\beta^+_N - \sqrt{2}\mathrm{i}\frac{\alpha_\mathrm{R}}{\hbar}\alpha^+_N\right] .\end{aligned} \tag{B.5}$$

The lower branch intraband transitions are specific with respect to the evolution of LLs. The energy of LLs decreases, however in a certain magnetic field they flip over and their energies start to increase, see Fig. 3.3. This implies transitions in both polarizations within this lower branch, therefore we have to calculate two sets of velocity matrix elements. The velocity matrix elements for the intraband inter-Landau level transitions within lower branch and σ^+ polarization are very similar to the previous ones except the complex coefficients:

$$\begin{aligned}&\langle N_- + 1|\widehat{v}_+|N_-\rangle = \\ &= \frac{\hbar}{m^*}\frac{\sqrt{N+1}}{l_B}\left(\alpha^-_{N+1}\right)^*\alpha^-_N + \left(\beta^-_{N+1}\right)^*\left[\frac{\hbar}{m^*}\frac{\sqrt{N}}{l_B}\beta^-_N - \sqrt{2}\mathrm{i}\frac{\alpha_\mathrm{R}}{\hbar}\alpha^-_N\right] .\end{aligned} \tag{B.6}$$

And finally, we give the the velocity matrix elements for the intraband inter-Landau level transitions within lower branch and σ^- polarization:

$$\begin{aligned}&\langle N_-|\widehat{v}_-|N_- + 1\rangle = \\ &= \left(\alpha^-_N\right)^*\left[\frac{\hbar}{m^*}\frac{\sqrt{N+1}}{l_B}\alpha^-_{N+1} + \sqrt{2}\mathrm{i}\frac{\alpha_\mathrm{R}}{\hbar}\beta^-_{N+1}\right] + \alpha^-_N + \frac{\hbar}{m^*}\frac{\sqrt{N}}{l_B}\left(\beta^-_N\right)^*\beta^-_{N+1} .\end{aligned} \tag{B.7}$$

BIBLIOGRAPHY

[1] P. D. C. King, R. C. Hatch, M. Bianchi, R. Ovsyannikov, C. Lupulescu, G. Landolt, B. Slomski, J. H. Dil, D. Guan, J. L. Mi, E. D. L. Rienks, J. Fink, A. Lindblad, S. Svensson, S. Bao, G. Balakrishnan, B. B. Iversen, J. Osterwalder, W. Eberhardt, F. Baumberger, and P. Hofmann. Large Tunable Rashba Spin Splitting of a Two-Dimensional Electron Gas in Bi_2Se_3. *Phys. Rev. Lett.* **107**, 096 802, 2011.

[2] C. R. Ast, J. Henk, A. Ernst, L. Moreschini, M. C. Falub, D. Pacilé, P. Bruno, K. Kern, and M. Grioni. Giant Spin Splitting through Surface Alloying. *Phys. Rev. Lett.* **98**, 186 807, 2007.

[3] G. Khodaparast, R. Doezema, S. Chung, K. Goldammer, and M. Santos. Spectroscopy of Rashba spin splitting in InSb quantum wells. *Phys. Rev. B* **70**, 155 322, 2004.

[4] M. Schultz, F. Heinrichs, U. Merkt, T. Colin, T. Skauli, and S. Løvold. Rashba spin splitting in a gated HgTe quantum well. *Semicond. Sci. Technol.* **11**, 1168–1172, 1996.

[5] C. Schierholz. *Rashba Spin-Orbit Interaction in Low and High Magnetic Fields*. CUVILLIER VERLAG, Göttingen, Germany, 2005.

[6] K. Ishizaka, M. S. Bahramy, H. Murakawa, M. Sakano, T. Shimojima, T. Sonobe, K. Koizumi, S. Shin, H. Miyahara, a. Kimura, K. Miyamoto, T. Okuda, H. Namatame, M. Taniguchi, R. Arita, N. Nagaosa, K. Kobayashi, Y. Murakami, R. Kumai, Y. Kaneko, Y. Onose, and Y. Tokura. Giant Rashba-type spin splitting in bulk BiTeI. *Nat. Mater.* **10**, 521–526, 2011.

[7] S. Bordács, J. G. Checkelsky, H. Murakawa, H. Y. Hwang, and Y. Tokura. Landau Level Spectroscopy of Dirac Electrons in a Polar Semiconductor with Giant Rashba Spin Splitting. *Phys. Rev. Lett.* **111**, 166 403, 2013.

[8] A. Akrap, A. Teyssier, J.and Magrez, P. Bugnon, H. Berger, A. B. Kuzmenko, and D. van der Marel. Optical properties of BiTeBr and BiTeCl. *Phys. Rev. B* **90**, 035 201, 2014.

[9] E. I. Rashba. Properties of semiconductors with an extremum loop. 1. Cyclotron and combinational resonance in a magnetic field perpendicular to the plane of the loop. *Sov. Phys. Solid State* **2**, 1224–1238, 1960.

[10] S. V. Eremeev, I. A. Nechaev, Y. M. Koroteev, P. M. Echenique, and E. V. Chulkov. Ideal Two-Dimensional Electron Systems with a Giant Rashba-Type Spin Splitting in Real Materials: Surfaces of Bismuth Tellurohalides. *Phys. Rev. Lett.* **108**, 246 802, 2012.

[11] Y. M. Koroteev, G. Bihlmayer, J. E. Gayone, E. V. Chulkov, S. Blügel, P. M. Echenique, and P. Hofmann. Strong Spin-Orbit Splitting on Bi Surfaces. *Phys. Rev. Lett.* **93**, 046 403, 2004.

[12] S. LaShell, B. A. McDougall, and E. Jensen. Spin Splitting of an Au(111) Surface State Band Observed with Angle Resolved Photoelectron Spectroscopy. *Phys. Rev. Lett.* **77**, 3419–3422, 1996.

[13] G. Lommer, F. Malcher, and U. Rossler. Spin splitting in semiconductor heterostructures for B→0. *Phys. Rev. Lett.* **60**, 728–731, 1988.

[14] J. C. Egues, G. Burkard, and D. Loss. Datta-Das transistor with enhanced spin control. *Appl. Phys. Lett.* **82**, 2658, 2003.

[15] L. Petersen and P. Hedegård. A simple tight.-binding model spin-orbit splitting of sp-derived surface states. *Surf. Sci.* **459**, 49–56, 2000.

[16] O. Krupin. *Dichroism and Rashba effect at magnetic crystal surfaces of rare-earth metals*. Ph.D. thesis. Freie Universität Berlin, Department of Physics, 2004.

[17] R. Winkler. *Spin-Orbit Coupling Effects in Two-Dimensional Electron and Hole Systems*. Springer-Verlag, Berlin, Germany, 2003.

[18] M. S. Bahramy, R. Arita, and N. Nagaosa. Origin of giant bulk Rashba splitting: Application to BiTeI. *Phys. Rev. B* **84**, 041 202, 2011.

[19] N. Goncharuk and L. Smrčka. Tight-binding description of Landau levels of graphite in tilted magnetic fields. *J. Phys. Condens. Matter* **24**, 185 503, 2012.

[20] P. Neugebauer, M. Orlita, C. Faugeras, A.-L. Barra, and M. Potemski. How Perfect Can Graphene Be? *Phys. Rev. Lett.* **103**, 136 403, 2009.

[21] M. Hitoshi. Landau Levels [Lecture notes]. 2006.
Available from http://hitoshi.berkeley.edu/221a/landau.pdf

[22] G. Li and E. Y. Andrei. Observation of Landau levels of Dirac fermions in graphite. *Nature Phys.* **3**, 623–627, 2007.

[23] A. K. Geim and A. H. MacDonald. Graphene: Exploring carbon flatland. *Phys. Today* **60**, 35–41, 2007.

[24] M. L. Sadowski, G. Martinez, M. Potemski, C. Berger, and W. A. de Heer. Landau level spectroscopy of ultrathin graphite layers. *Phys. Rev. Lett.* **97**, 266 405, 2006.

[25] K. S. Novoselov, A. K. Geim, S. V. Morozov, D. Jiang, M. I. Katsnelson, I. V. Grigorieva, S. V. Dubonos, and A. A. Firsov. Two-dimensional gas of massless Dirac fermions in graphene. *Nature* **438**, 197–200, 2005.

[26] G. Landolt, S. V. Eremeev, O. E. Tereshchenko, S. Muff, B. Slomski, K. A. Kokh, M. Kobayashi, T. Schmitt, V. N. Strocov, J. Osterwalder, E. V. Chulkov, and J. H. Dil. Bulk and surface Rashba splitting in single termination BiTeCl. *N. J. Phys.* **15**, 085 022, 2013.

[27] E. Dönges. Über Chalkogenohalogenide des dreiwertigen Antimons und Wismuts. III. Über Tellurohalogenide des dreiwertigen Antimons und Wismuts und über Antimon-und Wismut(III)-tellurid und Wismut(III)-selenid. *Z. Anorg. Allg. Chem.* **265**, 56–61, 1951.

[28] A. Tomokiyo, T. Okada, and S. Kawano. Phase Diagram of System (Bi_2Te_3) - (BiI_3) and Crystal Structure of BiTeI. *Jpn. J. Appl. Phys.* **16**, 1977.

[29] A. Shevelkov, E. Dikarev, R. Shpanchenko, and B. Popovkin. Crystal Structures of Bismuth Tellurohalides BiTeX (X = Cl, Br, I) from X-Ray Powder Diffraction Data. *J. Solid State Chem.* **114**, 379 – 384, 1995.

[30] Y. L. Chen, M. Kanou, Z. K. Liu, H. J. Zhang, J. a. Sobota, D. Leuenberger, S. K. Mo, B. Zhou, S. L. Yang, P. S. Kirchmann, D. H. Lu, R. G. Moore, Z. Hussain, Z. X. Shen, X. L. Qi, and T. Sasagawa. Discovery of a single topological Dirac fermion in the strong inversion asymmetric compound BiTeCl. *Nat. Phys.* **9**, 5, 2013.

[31] G. Landolt, S. V. Eremeev, O. E. Tereshchenko, S. Muff, K. A. Kokh, J. Osterwalder, E. V. Chulkov, and J. H. Dil. Direct measurement of the bulk spin structure of noncentrosymmetric BiTeCl. *Phys. Rev. B* **91**, 081 201, 2015.

[32] S. V. Eremeev, I. P. Rusinov, I. a. Nechaev, and E. V. Chulkov. Rashba split surface states in BiTeBr. *N. J. Phys.* **15**, 075 015, 2013.

[33] Z. Zhu, Y. Cheng, and U. Schwingenschlögl. Orbital-dependent Rashba coupling in bulk BiTeCl and BiTeI. *N. J. Phys.* **15**, 023 010, 2013.

[34] M. Sakano, M. Bahramy, a. Katayama, T. Shimojima, H. Murakawa, Y. Kaneko, W. Malaeb, S. Shin, K. Ono, H. Kumigashira, R. Arita, N. Nagaosa, H. Hwang, Y. Tokura, and K. Ishizaka. Strongly Spin-Orbit Coupled Two-Dimensional Electron Gas Emerging near the Surface of Polar Semiconductors. *Phys. Rev. Lett.* **110**, 107 204, 2013.

[35] J. S. Lee, G. a. H. Schober, M. S. Bahramy, H. Murakawa, Y. Onose, R. Arita, N. Nagaosa, and Y. Tokura. Optical Response of Relativistic Electrons in the Polar BiTeI Semiconductor. *Phys. Rev. Lett.* **107**, 117 401, 2011.

[36] L. Demkó, G. a. H. Schober, V. Kocsis, M. S. Bahramy, H. Murakawa, J. S. Lee, I. Kézsmárki, R. Arita, N. Nagaosa, and Y. Tokura. Enhanced Infrared Magneto-Optical Response of the Nonmagnetic Semiconductor BiTeI Driven by Bulk Rashba Splitting. *Phys. Rev. Lett.* **109**, 167 401, 2012.

[37] C. Bell, M. Bahramy, H. Murakawa, J. Checkelsky, R. Arita, Y. Kaneko, Y. Onose, M. Tokunaga, Y. Kohama, N. Nagaosa, Y. Tokura, and H. Hwang. Shubnikov-de Haas oscillations in the bulk Rashba semiconductor BiTeI. *Phys. Rev. B* **87**, 081 109, 2013.

[38] I. P. Rusinov, I. A. Nechaev, S. V. Eremeev, C. Friedrich, S. Blügel, and E. V. Chulkov. Many-body effects on the Rashba-type spin splitting in bulk bismuth tellurohalides. *Phys. Rev. B* **87**, 205 103, 2013.

[39] P. K. Chakraborty, G. C. Datta, and K. P. Ghatak. The simple analysis of the Burstein-Moss shift in degenerate n-type semiconductors. *Phys. B* **339**, 198–203, 2003.

[40] K. A. Kokh, S. V. Makarenko, V. A. Golyashov, O. A. Shegai, and O. E. Tereshchenko. Melt growth of bulk Bi2Te3 crystals with a natural p-n junction. *CrystEngComm* **16**, 581–584, 2014.

[41] MINERAL PROPERTIES: CLEAVAGE [online]. Accessed 03/17/2015. Available from http://www.minerals.net/resource/property/cleavage_fracture_parting.aspx

[42] The Essential Microtome Leica RM2125 RTS [online]. Accessed 03/17/2015. Available from http://www.leicabiosystems.com/specimen-preparation/sectioning/rotary-microtomes/details/product/leica-rm2125-rts-1/downloads/

[43] K. S. Novoselov, A. K. Geim, S. V. Morozov, D. Jiang, Y. Zhang, S. V. Dubonos, I. V. Grigorieva, and A. A. Firsov. Electric Field Effect in Atomically Thin Carbon Films. *Science* **306**, 666–669, 2004.

[44] F07xx - Standard Dicing Tape [online]. Accessed 03/23/2015.
Available from http://www.microworld.eu/standard-dicing-tape-F07xx/

[45] WF Film [online]. Accessed 03/23/2015.
Available from http://www.gelpak.com/products/wf-film/

[46] ICROS^{TM} tape [online]. Accessed 03/25/2015.
Available from http://www.mitsuichemicals.com/icr.htm

[47] Helix [online]. Accessed 03/31/2015.
Available from http://en.wikipedia.org/wiki/Helix

[48] The magnets [online]. Accessed 03/31/2015.
Available from http://lncmi-g.grenoble.cnrs.fr/spip.php?rubrique110&lang=en

[49] H. Murakawa, M. S. Bahramy, M. Tokunaga, Y. Kohama, C. Bell, Y. Kaneko, N. Nagaosa, H. Y. Hwang, and Y. Tokura. Detection of Berry's phase in a Bulk Rashba semiconductor. *Science* **342**, 1490–3, 2013.

[50] C.-R. Wang, J.-C. Tung, R. Sankar, C.-T. Hsieh, Y.-Y. Chien, G.-Y. Guo, F. C. Chou, and W.-L. Lee. Magnetotransport in copper-doped noncentrosymmetric BiTeI. *Phys. Rev. B* **88**, 081 104, 2013.

[51] C. Martin, E. D. Mun, H. Berger, V. S. Zapf, and D. B. Tanner. Quantum oscillations and optical conductivity in Rashba spin-splitting BiTeI. *Phys. Rev. B* **87**, 041 104, 2013.

[52] M. L. Sadowski, G. Martinez, M. Potemski, C. Berger, and W. A. de Heer. Magneto-spectroscopy of epitaxial graphene. *Int. J. Mod. Phys. B* **21**, 1145–1154, 2007.

[53] M. Orlita and M. Potemski. Dirac electronic states in graphene systems: optical spectroscopy studies. *Semicond. Sci. Technol.* **25**, 063 001, 2010.

[54] G. Feve, W. Oliver, M. Aranzana, and Y. Yamamoto. Rashba effect within the coherent scattering formalism. *Phys. Rev. B* **66**, 155 328, 2002.

LIST OF ABBREVIATIONS

Abbreviation	Definition
2DEG	Two dimensional electron gas
2DES	Two dimensional electron system
ARPES	Angle resolved photoemission spectroscopy
BiTeX	Bismuth-tellurohalides (X = I, Br, Cl)
CBM	Conduction band minimum
CNRS	Centre Nationale de la Recherche Scientific
DC	Direct current
EPR	Electron paramagnetic resonance
ESR	Electron spin resonance
FT-IR	Fourier Transform Infrared
IFS	Inner Fermi surface
IPM ASCR	Institute of Physics of Materials of the Academy of Sciences of the Czech Republic
LLs	Landau levels
LNCMI	Laboratoire National des Champs Magnétiques Intenses
LOR 3A	Lift-off resist 3A
OFS	Outer Fermi surface
PMMA	Poly(methyl methacrylate)
RSS	Rashba-type spin splitting
SdH	Shubnikov-de Haas (oscillations)
SOI	Spin-orbit interaction
VASP	Vienna ab-initio simulation package
VBM	Valence band maximum